CONJUGATE HARD X-RAY FOOTPOINTS IN THE 2003 OCTOBER 29 X10 FLARE: UNSHEARING MOTIONS, CORRELATIONS, AND ASYMMETRIES

Wei Liu[12], Vahé Petrosian[2], Brian R. Dennis[1], and Gordon D. Holman[1]

ABSTRACT

We present a detailed imaging and spectroscopic study of the conjugate hard X-ray (HXR) footpoints (FPs) observed with *RHESSI* in the 2003 October 29 X10 flare. The double FPs first move toward and then away from each other, mainly parallel and perpendicular to the magnetic neutral line, respectively. The transition of these two phases of FP *unshearing motions* coincides with the direction reversal of the motion of the loop-top (LT) source, and with the minima of the estimated loop length and LT height. The FPs show temporal *correlations* between HXR flux, spectral index, and magnetic field strength. The HXR flux exponentially correlates with the magnetic field strength, which also anti-correlates with the spectral index before the second HXR peak's maximum, suggesting that particle acceleration sensitively depends on the magnetic field strength and/or reconnection rate. *Asymmetries* are observed between the FPs: on average, the eastern FP is 2.2 times brighter in HXR flux and 1.8 times weaker in magnetic field strength, and moves 2.8 times faster away from the neutral line than the western FP; the estimated coronal column density to the eastern FP from the LT source is 1.7 times smaller. The two FPs have marginally different spectral indexes. The eastern-to-western FP HXR flux ratio and magnetic field strength ratio are anti-correlated only before the second HXR peak's maximum. Neither magnetic mirroring nor column density *alone* can explain the totality of these observations, but their combination, together with other transport effects, might provide a full explanation. We have also developed novel techniques to remove particle contamination from HXR counts and to estimate effects of pulse pileup in imaging spectroscopy, which can be applied to other *RHESSI* flares in similar circumstances.

Subject headings: acceleration of particles—Sun: flares—Sun: magnetic fields—Sun: X-rays

1. INTRODUCTION

In the classical picture of solar flares (CHSKP, Carmichael 1964; Hirayama 1974; Sturrock 1966; Kopp & Pneuman 1976), magnetic reconnection occurs high in the corona, resulting in plasma heating and particle acceleration. Some of the high-energy particles may be trapped in the corona by plasma turbulence (e.g., Petrosian & Liu 2004) and/or by magnetic mirroring (e.g., Melrose & White 1979; Leach 1984), where energetic electrons produce the hard X-ray (HXR) loop-top (LT) sources (e.g., Masuda et al. 1994; Petrosian et al. 2002; Sui & Holman 2003; Jiang et al. 2006; Battaglia & Benz 2006; Liu 2006). Some particles escape the acceleration region into interplanetary space and can contribute to solar energetic particle (SEP) events detected at 1 AU (e.g., Liu et al. 2004a; Krucker et al. 2007). A significant portion of the accelerated particles escape down magnetic field lines and produce bremsstrahlung HXRs (by electrons) or gamma-ray lines (by protons and other ions), primarily in the *thick-target* (Brown 1971; Petrosian 1973) transition region and chromosphere. This results in the commonly observed HXRs at the conjugate footpoints (FPs; Hoyng et al. 1981; Sakao 1994; Petrosian et al. 2002; Saint-Hilaire et al. 2008) of the flare loop. Consequent energy redistribution in the lower atmosphere along the

arcade of such loops produces ribbons seen in Hα and occasionally in white-light. As time proceeds, reconnection occurs at higher altitudes in the inverted-Y shaped configuration, and consequently the HXR FPs (Sakao 1994; Qiu et al. 2002; Liu et al. 2004b) and Hα ribbons (Švestka 1976) are usually seen to move away from each other, while the soft and hard X-ray LT sources are observed to move upward simultaneously at a comparable speed (Gallagher et al. 2002; Sui et al. 2004; Liu et al. 2004b). At the same time, an upward growing loop system can be seen in Hα (Zirin & Tanaka 1973), extreme ultraviolet (EUV, Gallagher et al. 2002), and soft X-ray (SXR; Pallavicini et al. 1975; Tsuneta et al. 1992). Details of reconnection and particle acceleration, however, remain largely unknown. X-ray observations of the LT and FP sources, particularly of their spatial, temporal, and spectral properties, combined with magnetic field measurements of the flare region, can provide critical information about how and where electrons are accelerated subsequent to magnetic reconnection.

Apparent motions of X-ray LT and FP sources can be understood as sequential excitations/formations of flare loops (e.g., Schrijver et al. 2006) when the primary reconnection site changes its location. Source motions deviating from the above classical picture have been observed, especially in the past decade: (1) The altitude of the HXR LT source was discovered by the *Ramaty High Energy Solar Spectroscopic Imager* (*RHESSI*) to decrease during the rise of the impulsive phase prior to the expected increase (Sui & Holman 2003; Sui et al. 2004; Liu et al. 2004a, 2008). Shrinkage of

[1] Solar Physics Laboratory, Code 671, Heliophysics Science Division, NASA Goddard Space Flight Center, Greenbelt, MD 20771; weiliu@helio.gsfc.nasa.gov
[2] Center for Space Science and Astrophysics, Department of Physics, Stanford University, Stanford, California 94305

loops was also observed in SXR (Švestka et al. 1987; Forbes & Acton 1996; Vršnak et al. 2006; Reeves et al. 2008), EUV (Li & Gan 2006), and microwave (Li & Gan 2005) during flares, and in SXR on the quiet Sun (Wang et al. 1997). (2) HXR FPs exhibit even more patterns of motion. Sakao et al. (1998) found that in 7 out of 14 flares observed by the *Yohkoh* Hard X-Ray Telescope (HXT) the FPs move away from each other, while in the rest of the flares the FP separation decreases (see also Fletcher & Hudson 2002) or remains roughly constant. Bogachev et al. (2005) extended this study to 31 *Yohkoh* flares and found that only 13% (type I) are consistent with the classical flare model showing double FPs moving away from and nearly perpendicular to the magnetic neutral line (NL), while 26% (type II) of the flares exhibit FPs moving mainly along the NL in antiparallel directions, 35% (type III) have FPs moving along the NL in the same direction (see also Krucker et al. 2003; Grigis & Benz 2005), and the remaining 26% show complex motion patterns. Their type II events are of particular interest as they suggest that flare loops excited or formed more recently during reconnection are less sheared[3] (e.g., see a review on *Hinitori* results by Tanaka 1987; Somov et al. 2002). Reduction of shear during flares has been observed for decades in the form of loops seen in Hα (Zirin & Tanaka 1973; Rust & Bar 1973) and EUV (Asai et al. 2003) with an increasing angle from the NL, or of apparent **unshearing** motions of FPs seen in Hα (Asai et al. 2003), EUV (Su et al. 2007), and HXRs (Sakao 1994; Masuda et al. 2001; Schmahl et al. 2006). (3) Recently Ji et al. (2006, 2007) found that the decrease of the (Hα and HXR) FP separation and shear occurred when the estimated height of the LT source decreases during the rise of the impulsive peak. This has spurred renewed interest by establishing the connection between the LT descending motion and the FP approaching motion with decreasing shear. LT descents reported in the past were usually observed in flares occurring near the solar limb where the LT height can be readily measured, but the FP motions in the east-west direction are obscured by projection effects. Flares close to disk center, like the one reported here, give an alternative perspective.

Correlations between a pair of conjugate HXR FPs are expected, since they are believed to be produced by high-energy electrons released from the same acceleration region. The relative timing of conjugate FPs was found to be simultaneous within an uncertainty of 0.1–0.3 s (Sakao 1994) based on *Yohkoh* Hard X-Ray Telescope (HXT) observations. For double FPs in tens of flares observed by the *Ramaty High Energy Solar Spectroscopic Imager* (*RHESSI*), temporal correlations in the HXR fluxes in two wide energy bands (25–50 and 50–100 keV) with a time resolution of 8 s were identified by Jin & Ding (2007). Spectral correlations at individ-

ual HXR peaks were investigated by Saint-Hilaire et al. (2008), who found power-law indexes that differed by <0.6. This spectral index difference is similar to that found by Sakao (1994), but smaller than the values as high as 1 or 2 reported by Petrosian et al. (2002), both based on analysis of *Yohkoh* HXT images.

Asymmetric FPs, i.e., conjugate FPs with different properties (HXR fluxes, magnetic field strengths, etc.) are commonly observed (e.g., Sakao 1994). This has been ascribed to asymmetric magnetic mirroring where a brighter HXR FP is associated with a weaker magnetic field (Li et al. 1997; Aschwanden et al. 1999; Qiu et al. 2001; Li & Ding 2004). This picture is consistent with observations at radio wavelengths where brighter microwave emission appears at the FP with the stronger magnetic field (e.g., Kundu et al. 1995; Wang et al. 1995). Exceptions to the mirroring scenario were reported by Goff et al. (2004), who found one third of 32 *Yohkoh* flares with an opposite trend, that is, the association of the brighter HXR FP with the stronger magnetic field. Falewicz & Siarkowski (2007) re-examined three exceptions in the sample of Goff et al. and attributed this opposite asymmetry to different column densities in the two legs of the flare loop, as also suggested by Emslie et al. (2003) and Liu (2006). Temporal variations of the flux asymmetry were found in a *Yohkoh* flare (Siarkowski & Falewicz 2004), and energy- and time-dependent variations were seen in a *RHESSI* flare (Alexander & Metcalf 2002). The latter were interpreted by McClements & Alexander (2005) as a consequence of an asymmetric, energy- and time-dependent injection of accelerated electrons.

Previous studies of conjugate HXR FPs, in general, suffered from limited time, spatial, and/or energy resolution and/or coverage of HXR emission, mainly restricted by the instrumental capabilities, or from lack of magnetic field measurements. We report here on a comprehensive study of the conjugate FPs in the 2003 October 29 X10 flare observed by *RHESSI* that overcomes many of the previous shortcomings. This flare provides a unique opportunity to track the spatial and spectral evolution of the double HXR FPs and their associated magnetic fields in great detail, and to study all three interrelated aspects: *unshearing motions*, *correlations*, and *asymmetries*. This flare occurred near disk center, where FP motions and line-of-sight magnetic field measurements have minimum projection effects. Its long (∼20 minutes) impulsive phase and high *RHESSI* count rates up to several hundred keV allow for a detailed study of variations both in time and energy. The flare was also well observed by the *Transition Region and Coronal Explorer* (*TRACE*), the *Solar and Heliospheric Observatory* (*SOHO*), and other spacecraft and many ground-based observatories. The rich database of multiwavelength observations and a wide range of literature covering different aspects of this event (e.g., Xu et al. 2004; Krucker et al. 2005) are particularly beneficial for this in-depth study.

We present the observations and data analysis in § 2. These include general *RHESSI* light curves, images, and imaging spectroscopy. We investigate in § 3 the two phases (fast and slow) of unshearing motions of the FPs and the associated LT motion. In § 4 we explore various correlations of the FPs, particularly of their HXR fluxes, spectral shapes, spatial variations, and magnetic

---

[3] Hagyard et al. (1984) defined the degree of magnetic shear as "the difference at the photosphere between the azimuths of a potential field and the observed vector field, where the potential field is the one satisfying the boundary conditions provided by the observed line-of-sight field". In this paper we use "shear" to mean the angle between the line connecting the two conjugate FPs (i.e., believed to be on the same magnetic loop) and the normal to the NL; our "shear angle" defined in this sense represents *apparent* shear, since we do not have accurate vector magnetic field measurements.

fields. Possible contributions to the HXR flux and spectral asymmetries are discussed in § 5, followed by our conclusions in § 6. A discussion of pulse pileup effects, technical details on coaligning images made by different instruments, a mathematical treatment of the asymmetric column density effect, and an estimate of the coronal column densities in the legs of the flare loop are given in Appendixes A, B, C, and D, respectively. Note that due to the particular circumstances of this flare, we employed new procedures to remove particle contamination from HXR light curves and to estimate effects of pulse pileup in imaging spectroscopy. These techniques, as a bonus of this paper, can be applied to other *RHESSI* flares in similar difficult circumstances that could not be analyzed before.

2. OBSERVATIONS AND DATA ANALYSIS

We present in this section general multiwavelength and *RHESSI* X-ray observations to indicate the context for our detailed discussions to follow on the conjugate FPs. The event under study occurred in AR 10486 (W5°S18°) starting at 20:37 UT on 2003 October 29, during the so-called Halloween storms (e.g., Gopalswamy et al. 2005). It was a *Geostationary Operational Environment Satellite* (*GOES*) X10 class, white-light, two-ribbon flare, which produced strong gamma-ray line emission (Hurford et al. 2006) and helioseismic signals (Donea & Lindsey 2005). It was associated with various other solar activity, including a fast ($\sim$2000 km s^{-1}) halo coronal mass ejections (CMEs), and heliospheric consequences. This was the first white-light flare observed at the opacity minimum at 1.6 μm, which corresponds to the deepest layer of the photosphere that can be seen (Xu et al. 2004, 2006). There were strong photospheric shearing flows present near the magnetic NLs in this active region prior to the flare onset (Yang et al. 2004), which may be related to the unusually large amount of free magnetic energy ($\sim$6 $\times 10^{33}$ ergs; Metcalf et al. 2005) stored in this AR. By analyzing Huairou and Mees vector magnetograms, Liu et al. (2007) proposed that this flare resulted from reconnection between magnetic flux tubes having opposite current helicities. This may be connected to the soft X-ray sigmoid structure and unshearing motions of HXR FPs found by Ji et al. (2008) during the early phase of the flare. Liu & Hayashi (2006), using potential field extrapolations from the *SOHO* Michelson Doppler Imager (MDI) observations, investigated the large-scale coronal magnetic field of AR 10486 and its high productivity of CMEs. Liu et al. (2006a) found remote brightenings more than 2×10^5 km away from the main flare site. Solar energetic particles (SEPs) were detected after this flare by *GOES* and the *Advanced Composition Explorer* (*ACE*).

Our goal in this paper is to understand the temporal and spectral variations of the asymmetric HXR FPs and their associated magnetic fields. We thus focus on HXR observations obtained by *RHESSI* and line-of-sight (LOS) photospheric magnetograms obtained by *SOHO* MDI. Vector magnetograms measured with chromospheric emission lines are more desirable for this study, as relevant magnetic mirroring may take place above the chromosphere where thick-target HXRs are produced. The only available vector magnetograms recorded during/near the flare time are Mees data, which, however,

has not yet been fully calibrated (K. D. Leka 2008, private communication) and thus is not used here. On the other hand, since this flare is close to disk center (W5°S18°), LOS MDI magnetograms provide a reasonable approximation of the photospheric field that is assumed to be proportional to the chromospheric field. Yet bear in mind that the field is likely tilted and can obscure the MDI measurement due to projection effects. It would have been interesting to examine microwave images which may show opposite FP asymmetry as in HXRs (Kundu et al. 1995). However, spectrograms of this flare obtained at the Owens Valley Solar Array (OVSA Gary & Hurford 1990) do not allow for image reconstruction due to poor data quality (J. Lee & C. Liu 2007, private communication), while Nobeyama was not observing (before local time 6 AM).

2.1. *Light Curves and X-ray Images*

RHESSI had very good coverage of this event. However, HXR counts, particularly at high energies ($\gtrsim$40 keV), were contaminated by counts produced by radiation belt particles bombarding the spacecraft from all directions. Particle-caused counts mainly influence the *rear* segments of *RHESSI* detectors (unshielded), while the *front* segments are less affected during the flare since they have a smaller volume ($\sim$0.14 that of the rear segments) and they stop most of the downward-incident flare photons <150 keV (Smith et al. 2002) that may exceed the number of particle counts. In addition, particle count rates are not modulated by the grids and appear as a DC offset in the modulation pattern, which is removed during image reconstruction (Hurford et al. 2002). Therefore, particles do not affect our analysis in this paper since it mainly relies on images made using front rate only.

We obtained the spatially integrated X-ray fluxes free from particle contamination in the following way. (1) At low energies (<30 keV), no correction is needed since ample flare counts dominate over particle counts. (2) At high energies (30–150 keV), we used the rear segment counts to estimate the contribution of particles to the front segments, since rear counts in this energy range are almost entirely produced by particles. To do this, we first selected a non-flare interval 20:42:40–20:47:40 UT on 2003 October 30, one day after the flare when the spacecraft was at approximately the same geomagnetic location, to get a background estimate. We obtained the background count rate spectra averaged over detectors 1, 3–6, 8, and 9 for front and rear segments separately, and calculated the front-to-rear count-rate ratio. (The ratio is close to the volume ratio $\sim$0.14 of the two segments, because particle bombardments are expected to be isotropic. Meanwhile, the weak energy dependence of the ratio, ranging from 0.08 at 30 keV to 0.14 at 150 keV, may be related to the geometry of the segments.) We then repeated this for the flare to accumulate front and rear segment count rate spectra for every 4 s interval from 20:37 to 21:07 UT. For each time and energy bin, the rear count rate was multiplied by the front-to-rear ratio at this energy obtained above and then subtracted from the front count rate. A sample of the count rates before and after this correction is shown in Figure 1. As expected, during the bulk of the flare duration between 20:40 and 21:00 UT, the estimated fractional particle

contamination is minimal (<15% of total counts, except up to 50% between 20:52 and 20:55 UT) at a lower energy (55–56 keV), and becomes more appreciable (up to 75% at ∼20:53:30 UT) at a higher energy (120–125 keV). Note that this technique cannot be used for energies ≲30 keV due to the threshold (lower-level discriminator) of the rear segments set at ∼20 keV (Smith et al. 2002).
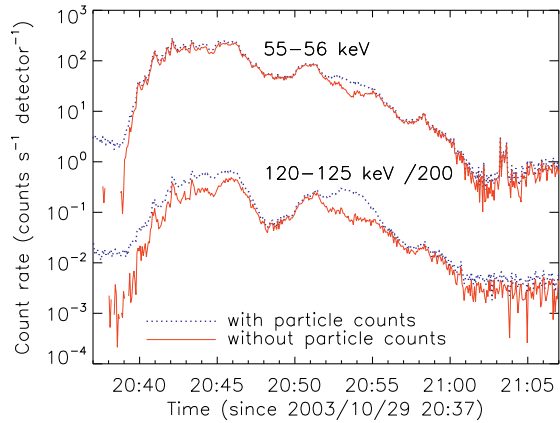

FIG. 1.— Count rates at two selected energies averaged over front segments 1, 3–6, 8, and 9 before (*dotted*) and after (*solid*) the correction for particle contamination. The 120–125 keV curves are scaled by a factor of 1/200.

The resulting X-ray count rates are also integrated in wide energy bands and are shown in Figure 2 together with *GOES* soft X-ray and OVSA microwave fluxes. We find that the *RHESSI* 80–120 keV and OVSA 16.4 GHz fluxes follow each other closely in time before 20:55 UT and both exhibit two major peaks (Peaks 1 and 2) divided at 20:48 UT. Note that the frequency at the maximum of the OVSA microwave spectrum is ≤11.2 GHz (except for three 4 s intervals between 20:41 and 20:44 UT when it reaches up to 14 GHz), and thus 16.4 GHz is on the optically-thin side of the spectrum which can be fitted with a power law.

TABLE 1
PHASES DURING THE COURSE OF THE FLARE.

	Phase I	Phase II
	20:40:40–20:44	20:44–20:59:40
FP unshearing motion	fast	slow
FP motion w.r.t. NL	parallel	perpendicular
LT altitude (estimated)	decrease	increase
	Peak 1	Peak 2
	20:39–20:48	20:48–21:02
mag. mirroring asymmetry	strong	weak
column densities in loops	small	large
FP B-fields correlation	exists	disappears

To obtain the flare morphology and its general evolution, we focused on a time range from 20:40:40 to 20:59:40 UT beyond which the double conjugate FPs of interest (identified below) were not clearly imaged, due to complex morphology and/or low count rates. We first divided this time range into 57 consecutive 20 s intervals, except for one interval that was shortened to 12 s to avoid the decimation state change at 20:46:36 UT. We then reconstructed images in two broad energy bands, 12–25 and 60-100 keV, using the CLEAN algorithm and
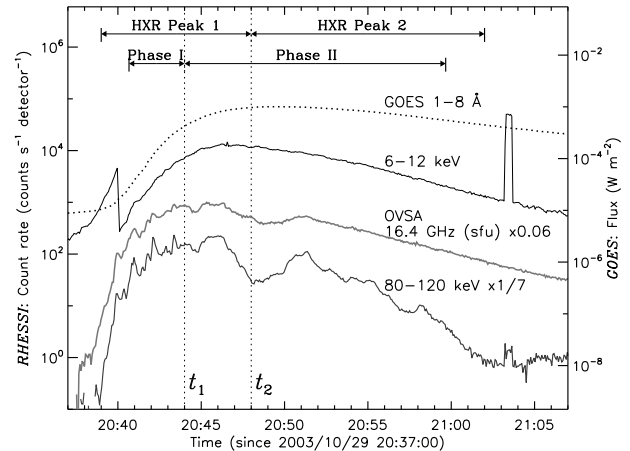

FIG. 2.— X-ray fluxes from *RHESSI* (6–12 and 80–120 keV, *left scale*) and *GOES*-12 (1–8 Å, *right scale*), and microwave flux (16.4 GHz, in sfu, *left scale*) from OVSA. The *RHESSI* fluxes are average count rates of front segments 1, 3–6, 8, and 9, with contamination from radiation belt particles removed. The artificial steps are due to attenuator state changes. The OVSA 16.4 GHz and *RHESSI* 80–120 keV curves are scaled by factors of 0.06 and $\frac{1}{7}$, respectively. The vertical dotted lines mark the two transitions, t_1 and t_2, where t_1 divides Phases I and II based on FP motions and t_2 divides two major HXR peaks (see Table 1). Count rates in the 20–50 keV range are affected pulse pileup and thus are not shown here.

uniform weighting among detectors 3–8 (Hurford et al. 2002). The effective FWHM angular resolution is 9.8″.

A sample of the resulting images is shown in Figure 3. Early in the flare (before 20:43:20 UT, Fig. 3*d*), several bright points at 60–100 keV are dispersed across the image, suggesting FPs of multiple loops. Part of the 12–25 keV emission appears elongated and curved between the adjacent FPs, corresponding to the LT source(s). Toward the south-west, part of the 12–25 keV emission seems to overlap with the FP emission, possibly due to a projection effect. As time proceeds, the FP structure seen at 60–100 keV becomes simpler, and only two distinct FPs are present (after 20:43:20 UT). They generally move away from each other. At the same time, the 12–25 keV emission gradually changes from one to two LT sources, one in the north and the other in the south.

We identified the conjugate FPs and the corresponding LT source of interest as follows for detailed analysis: (1) At later times (after 20:43:20 UT), only two FPs are seen in each image at 60-100 keV and so they are considered conjugate. We call the FP on the eastern (left) side E-FP and the one on the western (right) side W-FP (see, e.g., Fig. 3*h*). (2) At earlier times when more than two FPs are present, we set forth the following selection criteria: (*a*) The source morphology of the two conjugate FPs must be consistent with the picture that they are magnetically connected through the LT source between them seen in the corresponding 12–25 keV image (see, e.g., Fig. 3*b*). (*b*) During the time evolution the two FPs must show continuity and consistency in position and HXR flux, which other short-lived FPs lack. Under these criteria, the selected E-FP is the brightest FP to the east of the magnetic NL (*thick dashed* in Figs. 3*b* and 7*a*), and W-FP is the one to the west located nearest to the NL. (3) Once the conjugate FPs are found, their corresponding LT source was identified as the 12–25 keV emission that lies closest to the straight line joining the FPs. For example, at later times
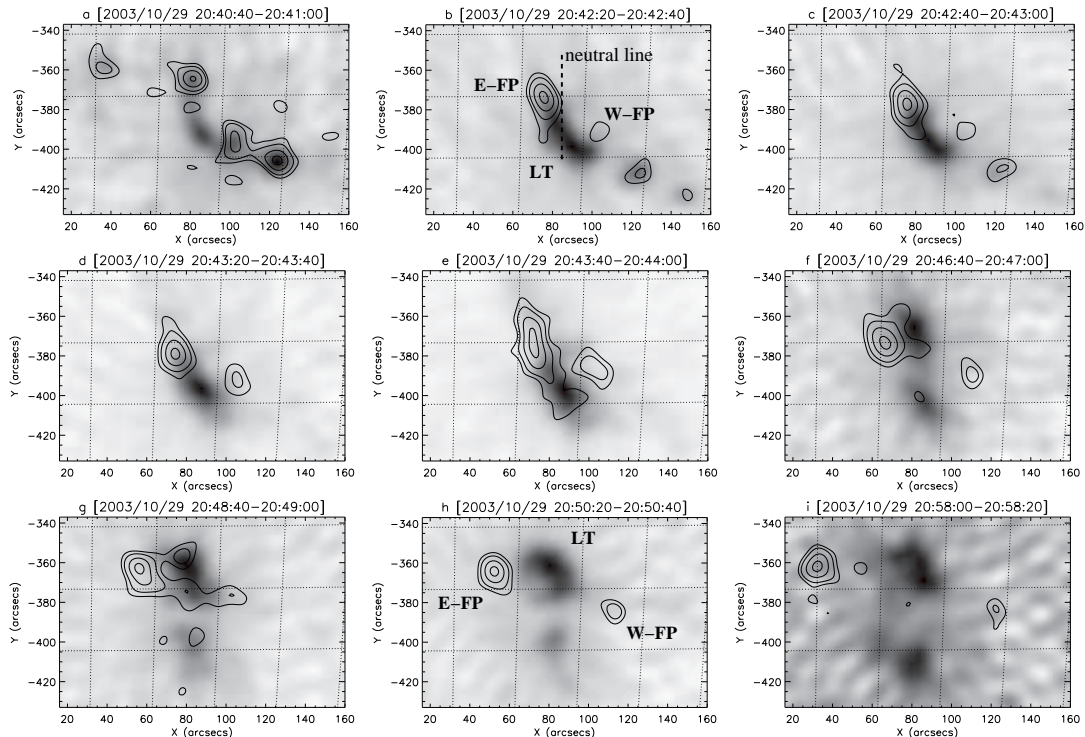
FIG. 3.— Evolution of HXR sources as seen in negative *RHESSI* CLEAN images made with detectors 3–8 (FWHM resolution 9.8″) in two energy bands, 12–25 keV as gray scale and 60–100 keV as contours (at 23%, 35%, 60%, and 90% of the maximum of each image). The dashed line in panel *b* shows the simplified magnetic NL also plotted in Fig. 7*a*. Correction for the solar differential rotation has been applied to this NL, and source centroids and images presented elsewhere in this paper when applicable unless otherwise noted.

(see, e.g., Fig. 3*h*), the northern LT is selected, while the southern LT is ignored since it does not seem to have any corresponding FP emission, presumably because of its faintness that exceeds *RHESSI*'s dynamic range ($\gtrsim$10:1 for images, Hurford et al. 2002; Liu 2006, p. 214 therein).

2.2. *Imaging Spectroscopy of Footpoint and Loop-top Sources*

Next, we examine the spectroscopic characteristics of the LT and FP sources and their temporal evolution. For each of the 57 consecutive 20 s intervals defined above, we reconstructed CLEAN images in 16 energy bins that are progressively wider from 6 to 150 keV. A sample of these images is shown in Figure 4 for 20:51:20–20:51:40 UT, where four images showing similar morphology as in neighboring energy bins are omitted. The emission is dominated by the two LT sources at low energies and the double FP sources at high energies.

The next step was to obtain photon fluxes of the sources for each time interval. For each FP source, we used a hand-drawn polygon that envelops all the 10% (of the maximum brightness of the image) contours at energies where this FP source was clearly imaged. For the corresponding LT source, we drew a polygon that encloses the 20% contours, which was selected to minimize spatial contamination from the FPs. We then read the resulting multiple-energy image cube into the standard *RHESSI* spectral analysis software (OSPEX) package. This package integrates photon fluxes inside each polygon, and uses the full detector response matrix to estimate the true incident photon spectrum. The RMS of the residual map of the CLEAN image was used to calculate the uncertainty for the photon flux in each energy bin, with proper consideration of the source area and grid

spatial resolution. This imaging spectroscopy technique is detailed by Liu et al. (2008). Note that we did not use contours at a fixed level (as opposed to polygons fixed in space) to obtain the fluxes because of the complex source morphology that makes such contours vary with energy.

One important issue for this X10 flare is pulse pileup (Smith et al. 2002) that at high count rates distorts the count-rate spectrum. We have discussed in Appendix A various effects of pileup on our analysis and the remedy that we have applied to minimize them. Although it is currently not possible to obtain accurate spectra throughout the full energy range for all sources, pileup mainly affects the LT spectra in the range of 20–50 keV (e.g., see Figs. 4*h* and 4*k*). In other words, pileup effects on spectral shapes are negligible for the LT sources below 20 keV and for the FP sources above 50 keV. This conclusion enabled us to confine the extent of pileup effects both in energy and in space. We thus fitted the LT spectrum below 20 keV with an assumed isothermal model from CHIANTI ver. 5.2 (Young et al. 2003), using the default coronal iron abundance of 4 times the photospheric value, to determine its temperature (T) and emission measure (EM); we fitted the FP spectrum above 50 keV with an assumed single power-law model to find its spectral index (γ) and normalization flux (I) at the reference energy of 50 keV.

Spectra of the LT and FP sources are shown in Figure 5*a* for the interval of 20:44:40–20:45:00 UT (during the main impulsive peak). Above 50 keV, both FP spectra have a power-law shape, with the E-FP flux being twice that of W-FP but only slightly harder. Consequently, the W-to-E ratio of the two FP spectra generally decreases with energy (Fig. 5*b*) or stays constant within uncertainties. Below 20 keV the LT spectrum shows the
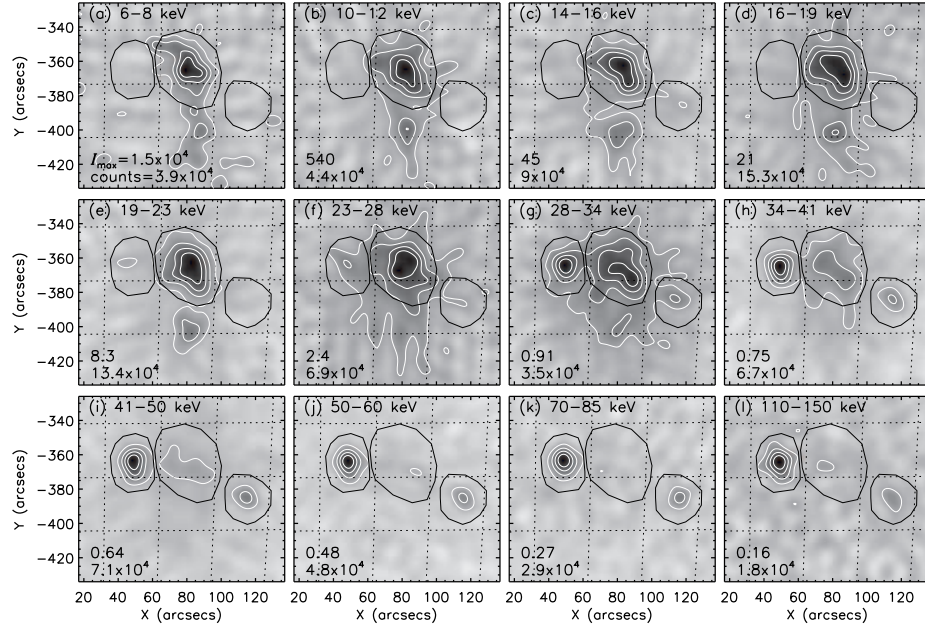
Liu et al.

FIG. 4.— negative CLEAN images in different energy bins at 20:51:20–20:51:40 UT made with detectors 3–9. The contour levels are 20%, 40%, 60%, and 80% of the maximum surface brightness, I_{max} (shown in the lower left corner of each panel, in units of photons cm^{-2} s^{-1} arcsec^{-2}), of each individual image. The number below I_{max} indicates the total counts accumulated by the detectors used. The same three dark, hand-drawn polygons in each panel were used to obtain the fluxes of the LT and two FP sources.
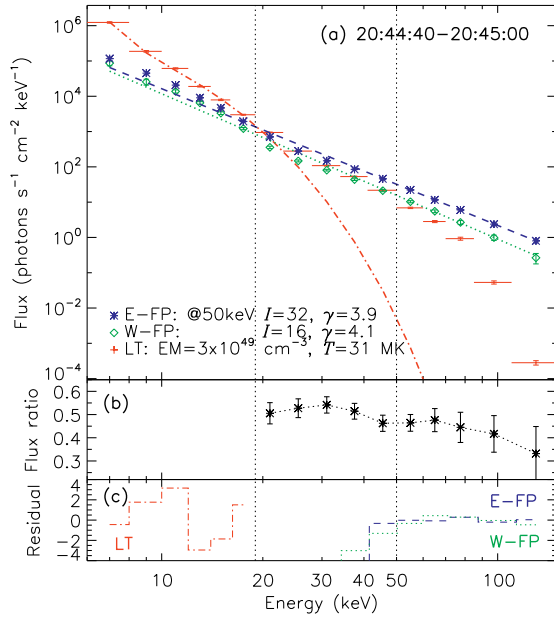

FIG. 5.— (a) Spatially resolved spectra of the LT and two FP sources at 20:44:40–20:45:00 UT. The horizontal bars on the LT spectrum represent the energy bin widths in the range of 6–150 keV. The dashed and dotted lines are power-law fits from 50–150 keV for E-FP and W-FP, respectively, and the dot-dashed line is a single temperature thermal fit from 6–19 keV for the LT. The legend shows the photon fluxes (I) at 50 keV and the spectral indexes (γ) for the FPs, and the emission measure (EM) and temperature (T) for the LT. (b) Ratio of the W-to-E FP fluxes. (c) Fitting residuals normalized by the 1σ uncertainties for the LT (dot-dashed), E-FP (dashed) and W-FP (dotted) sources.
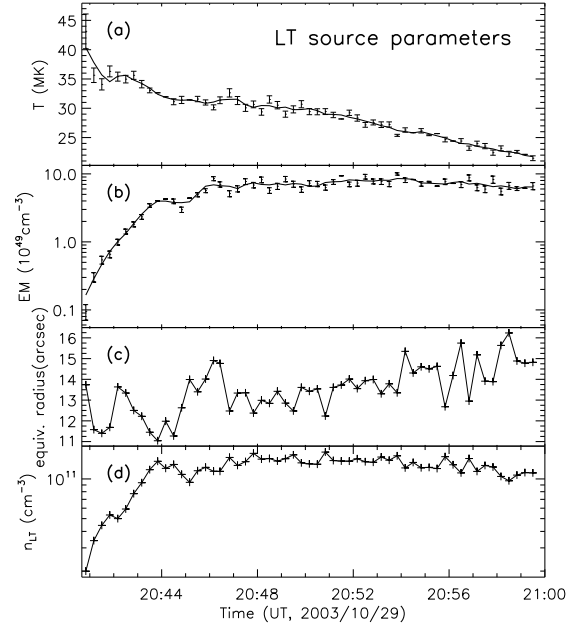

FIG. 6.— Evolution of spectroscopic parameters of the LT source. (a) Temperature T and (b) emission measure EM with 20 s integration time. The solid lines are 7-point box-car smooths of the original fitting results indicated by the symbols. (c) Radius r of the equivalent sphere of the LT source (see §2.2) and (d) corresponding electron number density n_{LT}.

exponential shape of isothermal bremsstrahlung emission, with the iron line feature at 6.7 keV visible. Note that below 50 keV the FP spectra may be compromised by pileup effects[4] and spatial contamination from the LT

source, and likewise above 20 keV the apparent LT flux is contaminated by FP emission at the same energy and by pileup from lower energies (Fig. 5a). We show in Figure 6 the spectral evolution of the LT source and defer that of the FP sources to § 4.1.

In order to infer the density of the LT source, we as-

[4] We note that the same power-law trends of the two FP spectra

extend below 50 keV down to ∼30 keV, suggesting that pulse pileup may have minimal effects on the spectral shapes of the FPs, and that our selection of 50 keV as the lower limit for reliable FP spectra is likely to be unnecessarily conservative.

sumed that it has a spherical shape with the projected area a equal to the area inside the 50% brightness contour at 12–25 keV. We then obtained the radius $r = (a/\pi)^{1/2}$ and volume $V = 4\pi r^3/3$ of the *equivalent sphere* and the corresponding density $n_{LT} = [\mathrm{EM}/(Vf)]^{1/2}$. In doing so we assumed a filling factor f of unity, which means the density obtained here would be a lower limit, and used the EM values smoothed with a 7-point box-car to minimize fluctuations possibly caused by the inevitable anti-correlation between T and EM during spectral fitting. The values of r and n_{LT} as functions of time are shown in Figures 6c and 6d, respectively. As evident, the size of the sphere stays roughly constant between $11''$–$16''$ and thus the density follows the same trend as the EM.

3. TWO-PHASE FOOTPOINT UNSHEARING AND LOOP-TOP MOTIONS

We now examine in detail the spatial evolution of the double FP sources and the corresponding LT source, by tracking the migration of their emission centroids. For each 12–25 image obtained in § 2.1 we used a contour at 50% of the maximum brightness of the LT source to locate its centroid, while for each 60–100 keV image we used a 90% contour of each conjugate FP. The reason for a higher contour level for the FPs (than the LT) is that the E-FP source spreads along the flare ribbon (see, e.g., Fig. 3e) and we need this brightest "kernel" to obtain the corresponding magnetic field strength at the FP (see §4.3). The resulting centroids are shown in Figure 7.

The background preflare MDI magnetogram in Figure 7a was corrected from *SOHO* L1 view to Earth view and shifted by $\Delta x = 4.5'' \pm 2.0''$ and $\Delta y = -2.8'' \pm 2.0''$ in the solar east-west (x) and south-north (y) directions, respectively, to match the *RHESSI* aspect believed to be have sub-arcsecond accuracy (Fivian et al. 2002). The required shifts were determined by cross-correlating MDI magnetic anomaly features (e.g., Qiu & Gary 2003; Schrijver et al. 2006) with HXR FPs, as described in Appendix B. The MDI map and all *RHESSI* centroids were corrected for the solar rotation and shifted to their corresponding positions at a common time (20:50:42 UT) in the middle of the flare. As is evident, E-FP is located in the negative (*dark*) polarity to the left of the simplified magnetic NL (*red dashed*), while W-FP is in the positive (*white*) polarity to the right.

In an attempt to correct for projection effects and to obtain the true 3D loop geometry, we assumed that the centroids of the LT and two FP sources at a given time are connected by a semi-circular loop. We then used the solar x and y coordinates of these three points in the sky plane to determine the size and the orientation of the semi-circle in 3D space, knowing that the FPs are located on the solar surface and the LT in the corona. A sample of the loops at selected times is shown in Figure 7b. We find that the inclination angle between the model loop and the vertical direction ranges from $14°$ to $63°$, and that the loop length (l_{total}; see Fig. 8a) generally first decreases and then increases with a minimum at 20:43:50 UT.

The LT centroids (*plus signs*) as shown in Figure 7b are situated at all times close to the NL (*red dashed*) as expected, and form two clusters, one in the south and the other in the north. As time proceeds, the LT centroid ap-

pears to move from the apex of one loop to another along the arcade seen in *TRACE* 195 Å (not shown). It first gradually moves southward until 20:43:30 UT (marked by the middle circle in Fig. 7b), when it starts to rapidly shift to the northern cluster and then continue moving northward at progressively lower speeds. This can be more clearly seen from its relative displacement projected onto the north-south NL as a function of time (Fig. 8b, Δy_{LT}). The height of the LT centroid estimated from the model loops is also shown in Figure 8b and exhibits a general decrease followed by an increase.

As to the FPs, in general, E-FP first moves southward and then turns to the east, while W-FP first moves northward and then turns to the west, as indicated by the thick arrows in Figure 7b. The evolution of the position of E-FP *relative* to W-FP is shown in Figure 7c. There is clearly a turning point which occurs at t_1=20:44 UT and divides the evolution of the FP positions into two phases: (1) Phase I (20:40:40–20:44:00 UT) when the two FPs generally move toward each other in a direction essentially parallel to the NL, (2) Phase II (20:44:00–20:59:40 UT) when the FPs move away from each other mainly perpendicular to the NL. According to Bogachev et al. (2005), this flare falls into their type II events during Phase I and then type III during Phase II. Another signature of this two-phase division is the morphological transition at 20:43:20 UT, before which there are multiple FP sources, but only two FPs present afterwards (see Fig. 3). Below we describe in detail the HXR source evolution in the two phases.

We further decomposed the distance between the FPs into two components: perpendicular and parallel to the NL as shown in Figure 8c, where the two phases are divided by the vertical dotted line at t_1. As can be seen, the parallel distance (*asterisks*) first rapidly decreases at a velocity of 108 ± 18 km s^{-1} given by the linear fit during Phase I; it then stays almost constant during Phase II with a slow increase (7 ± 1 km s^{-1}). In contrast, the perpendicular distance (*squares*) has a slow variation in Phase I (15 ± 13 km s^{-1}) and increases continuously at a velocity of 51 ± 1 km s^{-1} in Phase II. These velocities are comparable to those of the *TRACE* EUV FPs found by Schrijver et al. (2006) in the 2003 October 28 X17 flare that occurred in the same active region as the flare under study. From the speed ($\sim$60 km s^{-1}) and size ($<$1400 km) of EUV FPs, they inferred the crossing time of the FP diameter or the excitation time scale of the HXR-producing electron beam in a single flare loop to be $\lesssim$23 s.

Next we obtained the shear angle (θ; Fig. 7c) from the normal to the NL (parallel to the y-axis) to the W-to-E relative positional vector, which is shown as a function of time in Figure 8d. This angle exhibits a fast decrease (from $56°$ to $22°$) during Phase I and a slow decrease (down to $12°$) during Phase II. An independent study by Ji et al. (2008), with different identifications of the FPs in this flare and thus larger scatter, also found a similar decrease of the shear angle in two phases, which they referred to as *sigmoid* and *arcade* phases based on the X-ray morphology. The apparent unshearing motions of the HXR FPs indicate that the later reconnected magnetic field lines are less sheared. It can be seen that *TRACE* 195 Å loops corresponding to the HXR FPs at early times (not shown) are indeed highly sheared. Similar
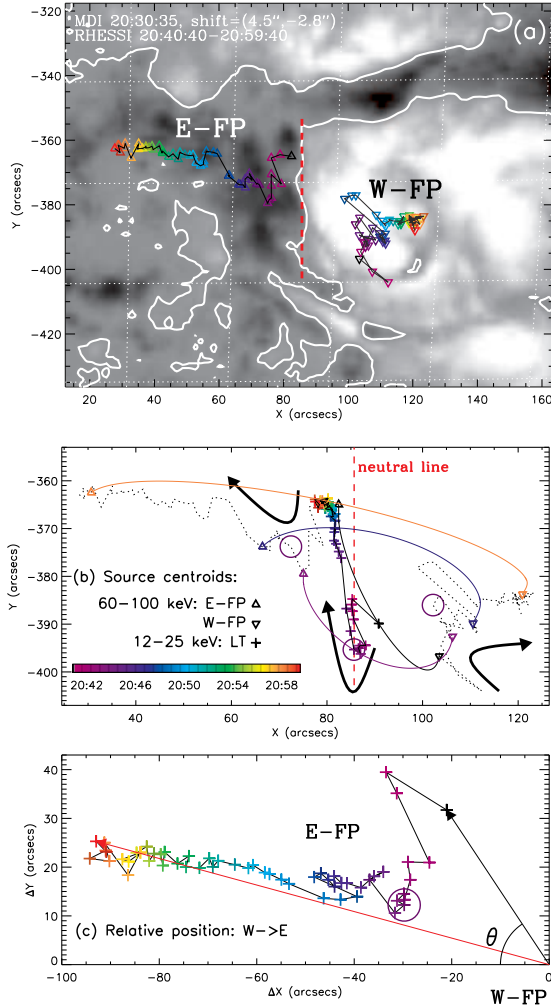
FIG. 7.— (*a*) preflare *SOHO* MDI magnetogram (centered at 20:30:35 UT with an integration time of 30 s) overlaid with magnetic NLs in white and the centroids of *RHESSI* FPs (E- and W-FP, at 60–100 keV) in color. The white (dark) gray scale represents positive (negative) line-of-sight magnetic fields pointing away (toward) the observer. The vertical red dashed line here and in (*b*) is the simplified NL that follows the observed magnetic NL between the two FPs. The temporal evolution at 20 s intervals of the *RHESSI* centroids is indicated by the color bar in (*b*). (*b*) Evolution of the centroid of the *RHESSI* LT source at 12–25 keV (*plus signs*). The tracks of the FP centroids shown in (*a*) are repeated here as dotted lines, along with positions at four selected times (labeled *a*, *d*, *f*, and *i* in Fig. 3) marked by triangles. We show semi-circular model loops at these times projected onto the sky plane, each of which connects three centroids (of two FPs & one LT) of the same color. The thick dark arrows indicate the general direction of motion for the LT and two FPs. (*c*) Relative centroid positions of E-FP with respect to W-FP which is selected as the origin. The start and end of the time evolution are marked by the black and red arrows. θ is the shear angle between the normal (due west) to the NL and the line joining the two FP centroids. The open circle here and those in (*b*) mark the transitional time t_1=20:44 UT from fast to slow unshearing motions of the FPs (see §3).

unshearing motions were observed in various wavelengths (e.g., Zirin & Tanaka 1973; Masuda et al. 2001; Su et al. 2007). Note that an opposite process took place prior to the flare, that is, strong photospheric shearing flows observed near the NL (Yang et al. 2004, as mentioned earlier). This process increased the shear of field lines and built up magnetic stress and free energy (Metcalf et al. 2005) in the system during the preflare phase.
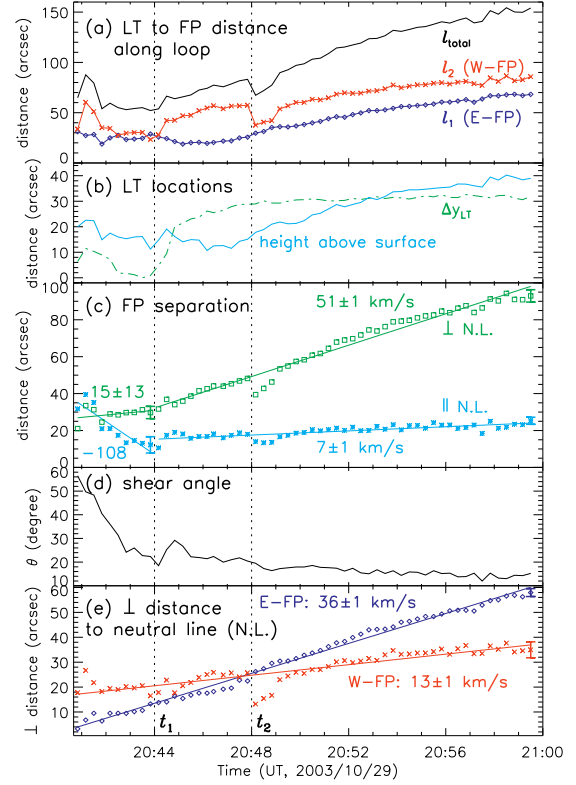

FIG. 8.— (*a*) History of distance (l_1 and l_2) from the LT centroid to the centroids of the two FPs along the semi-circular model loop as shown in Fig. 7*b*, together with the length of the loop ($l_{\rm total} = l_1 + l_2$). (*b*) Relative displacement ($\Delta y_{\rm LT}$, *dot-dashed*) of the LT centroid parallel to the magnetic NL shown in Fig. 7*b* and estimated height of the LT centroid above the solar surface (*solid*). (*c*) Orthogonal components of the separation between W-FP and E-FP perpendicular (*squares*) and parallel(*asterisks*) to the NL. The straight lines are linear fits to the distances in the two phases, labeled with the corresponding velocities (in km s^{-1}). (*d*) Shear angle θ defined in Fig. 7*c*. (*e*) Perpendicular distances to the NL from E-FP (*diamonds*) and W-FP (*crosses*). Linear fits for the whole flare duration are shown as the straight lines. The error bar shown on the last data point of each line here and in (*c*) is the RMS deviation of the data from the corresponding fit.

Finally we investigate the relationship between the FP and LT motions. The division at t_1=20:44 UT between the two phases of the FP unshearing motions coincides (within 30 s) with the minimum of the estimated loop length (Fig. 8*a*) and the direction reversal of the apparent LT motion (Fig. 8*b*) noted above. Also the estimated LT height undergoes a general decrease during Phase I when the HXR flux is on the rise. A similar decrease of the LT altitude during the rising portion of the impulsive phase, followed by a subsequent altitude increase, has been observed in many *RHESSI* flares near the limb (e.g, Sui & Holman 2003; Sui et al. 2004; Liu et al. 2004a, 2008; Holman et al. 2005). For those flares a complete physical picture is obscured because the observed FP motions are strongly subject to projection effects, but this drawback vanishes for the disk flare under study here. Assuming that our semi-circular model loops yield reasonable estimates of the LT heights and loop lengths, the above source motions, when taken together, suggest the following scenario: (1) During Phase I, as the the reconnection site and thus the LT source migrate southward along the NL or the arcade, shorter and less sheared loops are energized, which leads to the

apparent decrease of the LT altitude and the fast un-shearing motion of the FPs. (2) During Phase II, as the the reconnection site migrates northward at gradually lower speeds, longer and slightly less sheared loops are formed one above the other, and this results in the inferred increase of the altitude of the LT source and the separation of the FPs from the NL.

Phase II is in agreement with the classical CHSKP picture of two-ribbon flares, while Phase I is not. One possible physical explanation for Phase I[5] suggested by Ji et al. (2007) is the magnetic "implosion" conjecture (Hudson 2000) that predicts contraction of field lines during a flare as a consequence of explosive energy release. Ji et al. (2007) further found that a magnetic field with shorter, lower lying, and less sheared field lines indeed contains less free energy. Note that, in order to explain the LT descending motion, Veronig et al. (2006) proposed a collapsing magnetic trap model, which, however, cannot explain the initial FP motion toward one another parallel to the NL. In contrast, the scenario of Somov et al. (2002) for the approaching FPs does not predict the decrease of the LT height.

4. TEMPORAL CORRELATIONS OF CONJUGATE FOOTPOINTS

We now examine the temporal evolution of and correlations between various quantities of the two conjugate FPs, particularly spectral, spatial, and magnetic field parameters, which are summarized in Table 2.

4.1. Spectral Correlations

Figure 9a shows the history of the photon fluxes of E-FP (I_1, *blue diamonds*) and W-FP (I_2, *red crosses*) at 50 keV obtained from the power-law fits in the 50–150 keV range mentioned in § 2.2. We find that the two fluxes follow each other closely in their temporal trends and E-FP is always brighter than W-FP except for the first time interval. The correlation of the fluxes can also be seen in Figure 10a where one flux is plotted vs. the other. A linear regression is shown as the thick dashed line and given in Table 2. The correlation coefficients listed in Table 2 indicate a very high correlation in either a linear or a nonlinear sense. Such a correlation is expected for conjugate HXR FPs, since they are believed to be produced by similar populations of nonthermal electrons that escape the same acceleration region (believed to be at/near the LT source; Petrosian & Liu 2004; Liu et al. 2008) and travel down opposite legs of the same magnetic loop to reach the chromosphere.

We show the corresponding power-law indexes (γ) of the two FPs vs. time in Figure 9d and one index vs. the other in Figure 10b. Again we find that the two indexes are closely correlated, as can be seen from the large correlation coefficients (Table 2). The E-FP spectrum, however, is slightly harder than the W-FP spectrum, which it is persistent most of the time. The results from long integration intervals (2–3 minutes, not shown), which have better count statistics, exhibit the same pattern. We averaged the index values of the six 2 minute intervals covering 20:40:40–20:52:40 UT, after which the uncertainties

become large due to low count rates. This average gives $\langle \gamma_1 \rangle = 3.63 \pm 0.06$ for E-FP and $\langle \gamma_2 \rangle = 3.79 \pm 0.11$ for W-FP. Their difference of $\langle \gamma_2 \rangle - \langle \gamma_1 \rangle = 0.15 \pm 0.13$ is marginally significant at the 1σ level.

Let us compare the HXR fluxes and spectral indexes of the two FPs. As can be seen in Figures 9a and 9d, during HXR Peak 1 (before t_2=20:48 UT), the fluxes and indexes are anti-correlated, i.e., they follow the general "soft-hard-soft" (SHS) trend observed in many other flares (e.g., Parks & Winckler 1969; Kane & Anderson 1970). However, during Peak 2 (after t_2), the indexes decrease through the HXR maximum and then vary only slightly (with relatively large uncertainties) around a constant level of 3.0. This trend can be characterized as "soft-hard-hard" (SHH). This flux-index relationship can also be seen in Figure 10c where the index averaged between the two FPs is plotted against the average flux. Note that the spectral index values during the late declining phase of the flare are even smaller than those at the maximum of the main HXR Peak 1. In this sense, the overall spectral variation can be characterized as "soft-hard-soft-harder". As we noted earlier, there were energetic protons detected in interplanetary space by *GOES* and *ACE* following the flare. These observations, when taken together, are consistent with the statistical result of Kiplinger (1995) that this type of flare with progressive spectral hardening tends to be associated with SEP events (also see Saldanha et al. 2008). As we also noted, strong gamma-ray line emission was detected during this flare (Hurford et al. 2006), which indicates a significantly large population of accelerated protons at the Sun, but the relation to the SEPs at 1 AU is unclear.

4.2. Spatial Correlations

We now examine the spatial evolution of two FPs. In § 3 we focused on their relative motion, while here we compare their individual motions. Figure 8e shows the perpendicular distance of each FP from the north-south NL (*red dashed*, Fig. 7a) as a function of time. Linear fits of the full flare duration indicate mean velocities of $\langle v_\perp \rangle = 36 \pm 1$ for E-FP and $13 \pm 1 \, \mathrm{km \, s^{-1}}$ for W-FP. These velocities are similar to those found by Xu et al. (2004) for near infrared ribbons in this event. We also calculated the total velocities of the FP centroids, i.e., $v = (v_\perp^2 + v_\parallel^2)^{1/2}$, where $v_\perp$ and $v_\parallel$ are the components perpendicular and parallel to the NL, respectively. The two resulting velocities have a linear temporal correlation at a 5σ level (see Table 2), which again provides evidence of the causal connection between the conjugate FPs. However, the individual component, $v_\perp$ or $v_\parallel$, alone does not exhibit any noticeable correlation between the two FPs.

Figure 8a shows the distances from the LT centroid to the centroids of E-FP (l_1, *diamonds*) and W-FP (l_2, *crosses*) along the model semi-circular loop (see, e.g., Fig. 7b) as a function of time. Each curve follows the same general increase as the corresponding distance from the NL shown in Figure 8e, but the distance to E-FP is smaller than that to W-FP most of the time. We estimated the coronal column densities from the LT source to the transition region at the two FPs (see Appendix D for details) to be $N_{\mathrm{tr},\,i} = 0.5 n_{\mathrm{LT}}(l_i - r)$, where i=1, 2, using the distances l_i, LT density n_{LT} and equivalent ra-

---

[5] Considering the presence of multiple FPs (see Fig. 3), this phase might provide evidence for the tether-cutting model of Moore et al. (2001).

TABLE 2
Correlation coefficients and linear regressions between various parameters of the conjugate footpoints for the full flare duration (20:40:40–20:59:40 UT). Magnetic field strengths are in units of 100 Gauss.

Subscripts: 1: E-FP, 2: W-FP		r_p	# of σ's	r_s	signif.	Linear regression (between quantities in first two columns)
I_1	I_2	0.98	8	0.97	10^{-35}	$I_2 = (-0.3 \pm 0.1) + (0.41 \pm 0.01)I_1$
γ_1	γ_2	0.90	7	0.89	10^{-20}	$\gamma_2 = (-0.5 \pm 0.3) + (1.17 \pm 0.07)\gamma_1$
B_1	B_2	0.39	3	0.40	10^{-3}	$B_2 = (-9.2 \pm 0.8) + (3.7 \pm 0.1)B_1$
B_1	$\log_{10} I_1$	0.50	4	0.49	10^{-4}	$I_1 = (0.012 \pm 0.003) \times 10^{(0.55\pm0.02)B_1}$
B_2	$\log_{10} I_2$	0.82	6	0.84	10^{-16}	$I_2 = (0.19 \pm 0.01) \times 10^{(0.137\pm0.002)B_2}$
$\bar{B}$	$\log_{10} \bar{I}$	0.77	6	0.84	10^{-16}	$\bar{I} = (0.079 \pm 0.007) \times 10^{(0.252\pm0.005)\bar{B}}$
v_1	v_2	0.63	5	0.29	10^{-2}	$v_2 = (-93 \pm 10) + (2.8 \pm 0.1)v_1$

Note. — r_p: Pearson's linear correlation coefficient;
of σ's: multiple of 1σ uncertainty of r_p, where $\sigma = 1/(57)^{1/2} = 0.13$, in which 57 is the number of data points (or time intervals);
r_s and signif.: Spearman's rank correlation coefficient and significance level;
I (photons s^{-1} cm^{-2} keV^{-1}): HXR flux at 50 keV;
γ: spectral index between 50 and 150 keV (regression done only for 20:40:40–20:52:40 UT);
B (in 100 G): magnetic field;
$\bar{B}$ (in 100 G) and $\bar{I}$ (photons s^{-1} cm^{-2} keV^{-1}): B and I averaged between E-FP and W-FP;
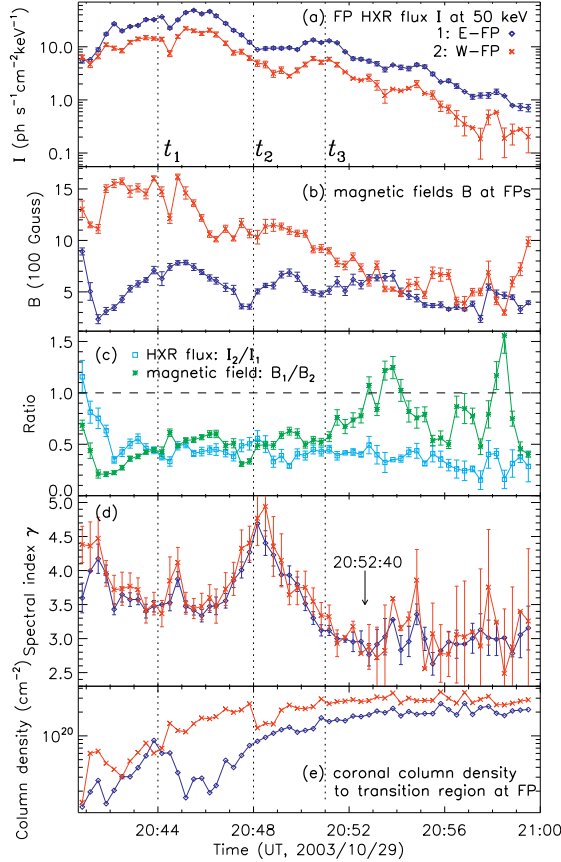v (km s^{-1}): FP velocity.

Fig. 9.— Time profiles of X-ray and magnetic field parameters. (a) HXR fluxes at 50 keV of E-FP (blue diamonds) and W-FP (red crosses) obtained from power-law fits in the 50–150 keV range. The same color and symbol convention for E- and W-FP holds for the other panels. The vertical dotted lines correspond to the transitional times of t_1 and t_2 as shown in Fig. 2, and t_3, the maximum of HXR Peak 2. (b) SOHO MDI magnetic field strengths registered at the two FPs. (c) Ratios of the 50 keV fluxes (W-to-E) and magnetic fields (E-to-W) of the two FPs. (d) HXR spectral indexes of the two FPs from the same fits as in (a). The arrow marks the end of the six 2 minute integration intervals for averaging the index values (see §4.1). (e) Estimated coronal column densities from the edge of the LT source to the transition region at the two FPs.
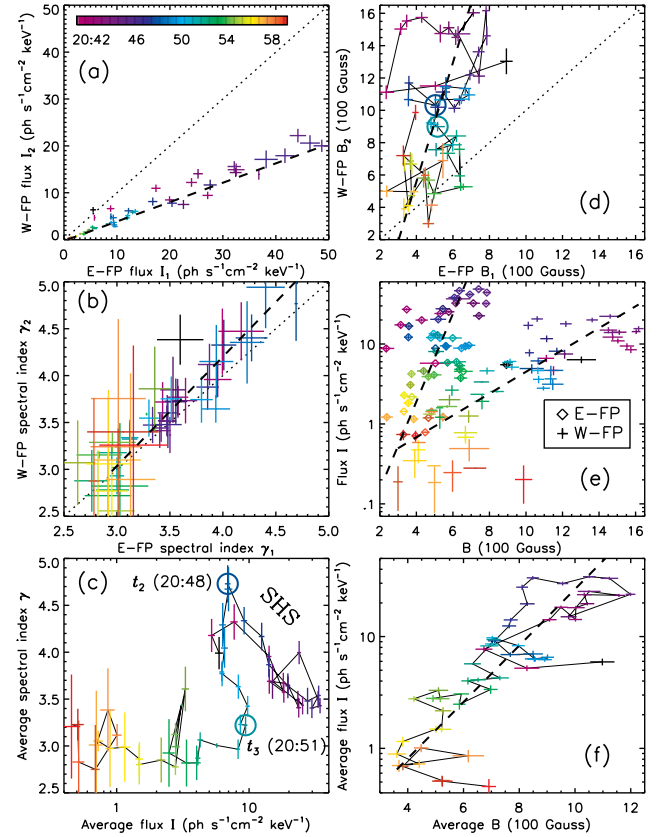
Fig. 10.— Various correlations between the HXR and magnetic field parameters of the two FPs. (a) HXR flux at 50 keV (Fig. 9a) of W-FP vs. E-FP. The dashed line here and in other panels represents a linear regression of the data. The color bar indicates the common time evolution for all panels of this figure. (b) Same as (a) but for the spectral indexes (γ) shown in Fig. 9d. The linear regression is done for the data points up to 20:52:40 UT. (c) Average (between the two FPs) spectral index $\bar{\gamma}$ vs. average flux $\bar{I}$ at 50 keV. The two open circles here and in (d) mark the times t_2 and t_3 shown in Fig. 9. A "soft-hard-soft" (SHS) variation is present early in the flare. (d) Same as (a) but for the magnetic field strengths of the two FPs as shown in Fig. 9b. (e) Logarithmic HXR flux at 50 keV vs. the corresponding magnetic field strength for E-FP (diamonds) and W-FP (plus signs). (f) Same as (e) but for the average values.

dius r obtained earlier (Fig. 6c). The results in Figure 9e show that there is a large relative difference from 20:44 to 20:48 UT during HXR Peak 1 but a smaller difference during Peak 2. Implications of these different column densities will be addressed in § 5.2 and § 5.3.

4.3. *Magnetic Field Correlation*

The magnetic field strengths of the two FPs were obtained from *SOHO* MDI magnetograms (e.g., see Fig. 7a) through the following steps: (1) We first selected a pre-flare[6] magnetogram at 08:30:35 UT and coaligned it with the *RHESSI* pointing and field of view using the offsets found in Appendix B. (2) For each time interval, the 90% brightness contour (not necessarily a resolved source) of each *RHESSI* FP source was rotated back to the corresponding position at the time of the MDI map to account for the solar rotation. Then the MDI pixels enclosed in this contour were averaged to give a value of the magnetic field for this FP, and the standard deviation of these pixels combined with the nominal 20 G MDI noise was used as the uncertainty. (3) The above two steps were repeated for each of the ten MDI magnetograms recorded between 20:25 and 20:35 UT at a one minute cadence (excluding the one at 20:28 UT that are contaminated by artificial pixel spikes). The average of the ten independent measurements was used as the final result for the magnetic field (Fig. 9b), and error propagation gave the final uncertainty ($\sim$5–10%).

As shown in Figure 9b, the magnetic field strength of W-FP generally decreases with time, while that of E-FP fluctuates about its mean value. Most of the time (especially before t_3=20:51 UT), the W-FP field is stronger than the E-FP field, while their fractional difference generally decreases as time proceeds. The temporal variations of the two field strengths are only weakly correlated (again, particularly before t_3) at the 3σ level (see Table 2), as can also be seen in Figure 10d.

4.4. *Inter-correlations Among Spectral, Spatial, and Magnetic Field Parameters*

Here we check the relationship between the HXR fluxes and the magnetic fields of the two conjugate FPs. We plot the logarithmic HXR flux vs. the magnetic field strength for each FP in Figure 10e. As we can see, the flux is correlated with the field strength for each FP (see Table 2 for the correlation coefficients and linear regressions). The logarithmic average flux ($\bar{I}$) and magnetic field ($\bar{B}$) of the two FPs are shown one vs. the other in Figure 10f. A linear relationship, as shown by the thick dashed line with a correlation coefficient of $r_p = 0.77 \pm 0.13$, is clearly present. In other words, $\bar{I}$ is exponentially (*nonlinearly*) correlated with $\bar{B}$, the expression of which is listed in Table 2. Since $\bar{I}$ is correlated with $\bar{B}$, the "soft-hard-soft" type of relationship between $\bar{\gamma}$ and $\bar{I}$ during the early phase (before t_3=20:51 UT)

translates to that between $\bar{\gamma}$ and $\bar{B}$. Namely, $\bar{\gamma}$ is anti-correlated with $\bar{B}$.

Finally we check the relationship of the apparent motions and magnetic fields of the two FPs. As noted above, E-FP moves faster than W-FP away from (perpendicular to) the magnetic NL, while E-FP is located in a weaker magnetic field. This relationship means that, as expected, about the same amount of magnetic flux is annihilated from each polarity, since $B\langle v_\perp \rangle$ is proportional to the magnetic reconnection rate. However, the magnetic fluxes swept by the two FPs, $\int B\langle v_\perp \rangle dt$ integrated over the full flare duration, differ by 44% of their average value. This is not surprising, as Fletcher & Hudson (2001) found a similar flux mismatch and offered various explanations.

4.5. *Discussion on Implications of Various Correlations*

The above correlation (Fig. 10f) between the average HXR flux and magnetic field strength reveals important information about the magnetic reconnection and particle acceleration processes. Here we speculate on two alternative possible scenarios in terms of contemporary acceleration theories.

1. The *nonlinear* (exponential) nature of the $\bar{I}$-$\bar{B}$ correlation suggests that particle acceleration is very sensitive to the magnetic field strength, if we assume that the measured photospheric field strengths scale with that in the coronal acceleration region. The stochastic acceleration model of Petrosian & Liu (2004) offers the following predictions: (1) The level of turbulence that determines the *number* of accelerated electrons is proportional to δB^2, where δB is the magnetic field amplitude of plasma waves. The acceleration rate that determines the spectral *hardness* of accelerated electrons is proportional to $\delta B^2/B$. An increasing field strength B will result in an increasing flux and spectral hardness of accelerated electrons, if both δB^2 and $\delta B^2/B$ also increase. (2) The relative efficiency of acceleration of electrons and thus their spectral *hardness* increase with decreasing values of the ratio of electron plasma frequency to gyro-frequency, $\alpha \equiv \omega_{pe}/\Omega_e \propto 1/B$. These predictions are qualitatively consistent with the observations that the magnetic field strength correlates with the HXR flux and anti-correlates with the spectral index.

2. Alternatively, noting the roughly constant velocities ($v_\perp$, Fig. 8e) of the two FPs perpendicular to the magnetic NL, the above $\bar{I}$-$\bar{B}$ correlation simply translates into the correlation between the HXR production rate and the magnetic flux annihilation rate or reconnection rate, $Bv_\perp$. Furthermore, since $Bv_\perp$ is believed to be proportional to the electric field in the reconnection region (Forbes & Lin 2000; Qiu et al. 2002), it then follows that the particle acceleration rate correlates with the electric field. According to the electric field acceleration model of Holman (1985) and Benka & Holman (1994), a larger electric field results in a larger high-energy cutoff ($E_{\max}$) for the electron spectrum, which can lead to a harder HXR spectrum (Holman 2003). This is consistent with the observed anti-correlation between the magnetic field strength and spectral index. Note that in the classical (Petschek 1964) model, the small cross-section of the current sheet cannot account for the typically large flux of accelerated electrons of 10^{34}–10^{37} electrons s^{-1} (Miller et al. 1997), i.e., the so-called "number

---

[6] Note that magnetograms during the flare cannot be used due to temporary artificial changes in the measured field strength (see Appendix B). Permanent real changes have been observed before and after many X-class flares (e.g., Wang et al. 2002; Sudol & Harvey 2005), and have been interpreted as magnetic field changes in direction rather than in strength (Sudol & Harvey 2005). Consequently we use the preflare field as the best approximation available to us for the field during the flare.

problem". However, observations and magnetohydrodynamic simulations (e.g., Kliem et al. 2000) have implied that the reconnecting current sheet involves small-scale electric fields around multiple, spatially separated magnetic X- and/or O-points in a fragmented topology (see a review by Aschwanden 2002). We speculate that, when particle acceleration takes place in such a fragmented current sheet, the number problem can be ameliorated (also see a discussion by Hannah & Fletcher 2006). In this case, the above discussion remains valid if the small-scale electric fields are scaled with the macroscopic potential drop and thus with $Bv_\perp$. For comparison, we note that Krucker et al. (2005) studied the motion of E-FP *alone* in this flare and also found a rough temporal correlation between the HXR flux and reconnection rate, represented by Bv or B^2v, where v includes the velocity both perpendicular and parallel to the NL.

5. HARD X-RAY FOOTPOINT ASYMMETRIES

As mentioned above and partly noted by Liu et al. (2004c), Xu et al. (2004), and Krucker et al. (2005), the two conjugate FPs exhibit the following asymmetric characteristics: (1) the *brighter* E-FP is located in a *weaker*, negative magnetic field, while the *dimmer* W-FP is located in a *stronger*, positive field; (2) the two FPs have very similar spectral shapes with E-FP being slightly harder; (3) E-FP is located *closer* to the LT than W-FP; (4) E-FP moves *faster* away from the magnetic NL than W-F. These asymmetries are summarized in Table 3.

We explore in this section different possibilities that can cause such asymmetries, particularly the asymmetric HXR fluxes and spectra. Various physical processes can contribute and they fall into two categories according to their origins: (1) asymmetry during particle acceleration, and (2) asymmetry arising from particle transport. The second category includes effects of magnetic mirroring and column density, which will be examined in what follows (§5.1–5.2). Other transport effects and the first category will be discussed later in § 5.4. We use both the flux ratio $R_I \equiv I_2/I_1$ and the asymmetry (c.f., Aschwanden et al. 1999) defined by Alexander & Metcalf (2002):

$$A \equiv (I_1 - I_2)/(I_1 + I_2) = (1 - R_I)/(1 + R_I), \quad (1)$$

to quantify the asymmetric HXR fluxes, with $A = \pm 1$ being 100% asymmetry and $A = 0$ being perfect symmetry.

5.1. *Magnetic Mirroring*

Asymmetric magnetic mirroring is commonly cited to explain asymmetric HXR fluxes observed at conjugate FPs. We examine to what extent mirroring alone can explain the observations of this flare. For simplicity, we make the following assumptions for our analysis below: (1) Disregard all non-adiabatic effects of particle transport, i.e., energy losses and pitch-angle diffusion due to Coulomb collisions. By this assumption, the magnetic moment of a particle is conserved and mirroring is the only effect that changes the pitch angle when the particle travels in the loop and outside the acceleration region. (2) Assume an isotropic pitch-angle distribution of the electrons at all energies upon release from the acceleration region. (3) Disregard details of bremsstrahlung, and

TABLE 3
ASYMMETRIC CHARACTERISTICS OF THE CONJUGATE FOOTPOINTS (E-FP AND W-FP): MEAN, MEDIAN, AND THEIR E-TO-W RATIO OF VARIOUS QUANTITIES.

	Mean			Median		
	E	W	E/W	E	W	E/W
I	13.7	6.1	2.2	8.9	4.6	1.9
B	520	960	0.55	520	1010	0.51
γ	3.63	3.79	0.96	3.4	3.5	0.96
l	41	60	0.69	38	60	0.64
$N_{\rm tr}$	1.2	2.1	0.60	1.2	2.5	0.50
$v_\perp$	36	13	2.8	—	—	—

NOTE. — I (photons s^{-1} cm^{-2} keV^{-1}): HXR flux at 50 keV;
B (Gauss): magnetic field strength;
γ: spectral index between 50 and 150 keV;
l (arcsecs): distance from the LT centroid to the FP centroid along the semi-circular loop;
$N_{\rm tr}$ (10^{20} cm^{-2}): coronal column density from the edge of the LT source to the transition region at the FP.
$v_\perp$ (km s^{-1}) : velocity perpendicular to the NL;
The mean spectral indexes are the averages of the results of the six 2 minute integration intervals between 20:40:40 and 20:52:40 UT (see §4.1), while all the other values listed here are from the results of the 57 short intervals throughout the flare.

assume that the nonthermal HXR flux is proportional to the precipitating electron flux at the FP.[7]

The loss-cone angle for magnetic mirroring is given as $\theta_i = \arcsin(B_0/B_i)^{1/2}$, (i=1 for E-FP, 2 for W-FP), where B_0 is the magnetic field strength at the injection site in the corona where particles escape from the acceleration region, and B_i is the field strength at the ith FP in the chromosphere. By the isotropy assumption, the fractional flux of the forward moving electrons that will *directly* precipitate to the chromosphere (whose pitch angle is located inside the loss cone) can be evaluated by integrating over the solid angle (also see Alexander & Metcalf 2002):

$$F_i = \frac{1}{2\pi} \int d\Omega = \frac{1}{2\pi} \int_0^{2\pi} d\phi \int_0^{\theta_i} \sin\theta d\theta = 1 - \mu_i, \quad (2)$$

where the pitch-angle cosine is $\mu_i = \cos\theta_i = (1 - B_0/B_i)^{1/2}$. If there is strong mirroring, i.e., $B_0 \ll B_i$, we have $\mu_i \simeq 1 - B_0/(2B_i)$, and if there is no mirroring, i.e., $B_0 = B_i$, we have $\mu_i = 1$. By our assumptions (1) and (3) above, such a fraction should be independent of electron energy and is proportional to the HXR flux I_i at the corresponding FP. It then follows that

$$R_I \equiv \frac{I_2}{I_1} = \frac{F_2}{F_1} = \frac{1 - \mu_2}{1 - \mu_1} \quad (3)$$

$$\simeq \begin{cases} \frac{B_1}{B_2} \equiv R_B^{-1}, & \text{if } B_0 \ll B_i, (i = 1, 2), \\ \frac{B_1}{2B_2} \equiv R_B^{-1}/2, & \text{if } B_0 = B_1, B_0 \ll B_2, \end{cases} \quad (4)$$

the second case of which corresponds to the possibility that mirroring occurs only at one FP, but the required condition $B_1 \ll B_2$ does not apply to this flare. In either

---

[7] This flux includes the precipitation of electrons previously reflected by mirroring back to the acceleration region at the LT where they may be scattered and/or re-accelerated, presumably by turbulence.

case, the HXR flux ratio should be correlated with the inverse of the magnetic field ratio, R_B^{-1}. This result is consistent with that of the strong diffusion case obtained by Melrose & White (1981).

As shown in Table 3, the mean/median HXR flux of E-FP is about twice that of W-FP, while the mean/median magnetic field strength of E-FP is about a factor of two smaller. This is consistent with the mirroring effect in the average sense of the whole flare duration. We can check if this relationship also holds at different times. Figure 9c shows the W-to-E ratio ($R_I = I_2/I_1$) of the HXR fluxes and the E-to-W ratio ($R_B^{-1} = B_1/B_2$) of the field strengths of the two FPs as a function of time. We find a temporal correlation between the two ratios during the first ~3 minutes when both first decrease and then increase. In the middle stage (20:43–20:51 UT) of the flare, both ratios remain roughly constant with marginal fluctuations and similar mean values of $\langle R_I \rangle = 0.43$ and $\langle R_B^{-1} \rangle = 0.50$. After 20:51 UT, the magnetic field ratio increases significantly with large fluctuations and exceeds unity in 6 of the 57 time intervals, while the flux ratio remains at about the same level as before. The behavior of the two ratios before 20:51 UT is expected from magnetic mirroring, but their significant difference after 20:51 UT cannot be explained by mirroring alone.

5.2. Column Density

Another transport effect that can cause asymmetric HXR FPs is different coronal column densities experienced by electrons in traveling from the acceleration region to the transition region at the two FPs (Emslie et al. 2003; Liu 2006, p. 73). The effective column density is $N_{\mathrm{tr, eff}} = N_{\mathrm{tr}}/\langle \mu \rangle$, where $\langle \mu \rangle$ is the average pitch angle cosine, and $N_{\mathrm{tr}} = \int_0^{s_{\mathrm{tr}}} n(s)ds$ is the coronal column density to the transition region at distance $s = s_{\mathrm{tr}}$ along the magnetic field line with $n(s)$ being the ambient electron number density. A difference in $\langle \mu \rangle$, s_{tr}, and/or $n(s)$ between the two legs of the flare loop can lead to different effective column densities. (1) Different pitch-angle distributions can be caused by asymmetric magnetic mirroring and/or asymmetric acceleration. (2) Different path lengths s_{tr} can be caused by a magnetic reconnection site located away from the middle of the loop (Falewicz & Siarkowski 2007). (3) Different densities $n(s)$ can also occur because magnetic reconnection takes place between field lines that are previously not connected and their associated densities are not necessarily the same. It takes time (on the order of the sound travel time, $\gtrsim$ tens of seconds) for the newly reconnected loop to reach a density equilibrium, but the observed HXRs could be produced before then.

Column density asymmetry affects the FP asymmetry in two ways, since both energy losses and pitch-angle scattering due to Coulomb collisions take place at about the same rate that is proportional to the column density: (1) Column density asymmetry is related to energy losses and the way we calculate the FP photon flux in § 2.2 (integrating HXR photons primarily produced below the transition region). Electrons with an initial energy of E are stopped after traveling through a column density $N_{\mathrm{stop}}(\mathrm{cm}^{-2})/ \approx 10^{17}[E(\mathrm{keV})]^2$. If N_{stop} is smaller than or comparable to the column density to the transition region (N_{tr}), in one half of the loop with a *larger* column

density, there are *more* electrons stopped in the leg and thus less electrons reaching the transition region. This results in *more* HXRs produced in the leg and less HXRs beneath the transition region (counted as the FP flux). (2) Different Coulomb scattering rates result from different column densities on the two sides of the loop, which can cause different pitch-angle distributions, even if the particles are injected with symmetrical pitch angles from the acceleration region.

Focusing on the energy dependence of FP HXR asymmetry, we present below an estimate of the column density effect *alone*, while assuming no magnetic mirroring and identical pitch-angle distributions (same $\langle \mu \rangle$) in the two loop legs. The relevant formulae are derived in Appendix C. We further assumed that identical power-law electron fluxes with a spectral index δ are injected into the two legs of the flare loop, which have the same ambient density but different path lengths s_{tr} to the FPs. Our goal is to examine if this scenario can yield photon fluxes and spectra consistent with observations for both FPs. For each of the 57 time intervals shown in Figure 9, we first used the E-FP column density N_{tr} (see §4.2 and Fig. 9e) from the edge of the LT source (assumed to be the acceleration region) to obtain its dimensionless form $\tau_{\mathrm{tr}} = N_{tr}/(5 \times 10^{22}\,\mathrm{cm}^{-2})$, which ranges from 5×10^{-4} to 1×10^{-2}. We then substituted τ_{tr} into

$$I_{\mathrm{FP}}(\tau_{\mathrm{tr}}, k) = A_0 k^{-(\delta-1)} \left(1 + \tau_{\mathrm{tr}} \frac{k+1}{0.37k^2}\right)^{1-\delta/2}, \quad (5)$$

rewritten from equation (C4), where A_0 is the normalization for the thick-target flux and k is the photon energy in units of the rest electron energy 511 keV. With this equation, we fitted the E-FP spectrum above 50 keV in a least-squares sense by iteratively adjusting the free parameters A_0 and δ. Using the resulting A_0 and δ and W-FP's τ_{tr}, we then calculated the W-FP spectrum by equation (5) and the W-to-E flux ratio by equation (C5).

Figure 11a shows an example of the spectra of the two FPs and their model predictions, together with the corresponding thick-target spectrum produced by the same power-law electron flux. We only trust the observed FP spectra >50keV due to pileup, as noted earlier. As expected, the model FP fluxes are reduced from the thick-target flux, especially at low energies, because low-energy electrons are more susceptible to collisional energy loss and pitch-angle scattering. This results in a spectral flattening (hardening) in the FP X-ray spectrum. Because of its larger column density, the W-FP's model spectrum exhibits more flux reduction at a given energy and a flattening to a higher energy. Above 50 keV the model spectrum of the brighter E-FP fits the data very well. However, that of the dimmer W-FP does not fit the data at all, since the model flux is much greater (e.g., at 77.5 keV $I = 4.0$ vs. 2.6 photons s^{-1} cm^{-2} keV^{-1}) and harder ($\gamma = 3.5$ vs. 4.1) than the observed flux, and even harder than the E-FP flux ($\gamma = 3.5$ vs. 3.9). This can be best seen in Figure 11b that shows the data (*plus signs*) and model (*solid line*) ratios of the W-to-E FP flux. The data ratio generally decreases with energy or stays roughly constant above 50keV within uncertainties, but the model ratio is an increasing function of energy. These trends generally hold throughout the flare as can be seen from the history of HXR fluxes and spectral indexes shown in Figures 11c and 11d.
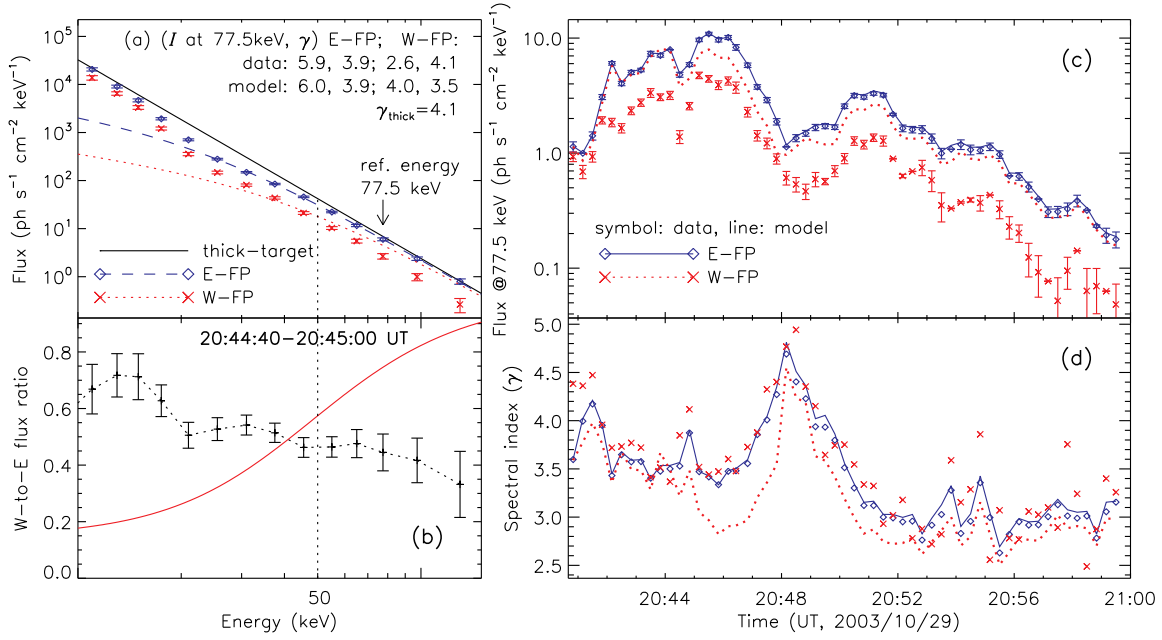
FIG. 11.— Effects of asymmetric coronal column densities. (*a*) Photon fluxes of E-FP (*diamonds*) and W-FP (*crosses*) vs. energy at 20:44:40–20:45:00 UT (same as Fig. 5*a*), superimposed with model fluxes (*lines*) evaluated below the transition region using eq. (5). The solid line shows the power-law thick-target flux with an index of $\gamma_{\text{thick}} = 4.1$. The legend shows the fluxes (I) at a reference energy of 77.5 keV and the spectral indexes (γ) above 50 keV of the two FPs for both the data and model. (*b*) Ratio of the W-to-E FP fluxes shown in (*a*), with the plus signs for the data and the solid line for the model (given by eq. C5). (*c*) Observed (*symbols*) and modeled (*lines*) fluxes of E- and W-FP at 77.5 keV vs. time (cf. Fig. 9*a* at 50 keV). (*d*) Same as (*c*) but for the spectral indexes above 50 keV. The data is the same as in Fig. 9*d* but without error bars for clarity.

In summary, the model predicts a much harder photon spectrum for the dimmer W-FP with the larger coronal column density, while according to the observations the dimmer W-FP is as hard as or slightly softer than the brighter E-FP (see Fig. 11*d*). Saint-Hilaire et al. (2008) reported similar results that the majority of the brighter FPs in their 172 pairs of FPs during the HXR peaks of 53 flares tend to have harder spectra. In addition, the differences between the model HXR fluxes of the two FPs are too small to explain the observations (Fig. 11*c*). One may attempt to increase the difference between the column densities in order to increase the flux difference and thus to merge this gap between the model and data, but the discrepancy of the spectral indexes would be exacerbated since the W-FP spectrum would be relatively even harder. Therefore, we conclude that the column density effect alone cannot provide a self-consistent explanation for both the HXR fluxes and spectra of the asymmetric FPs observed here.

Falewicz & Siarkowski (2007), however, found in three flares that the HXR flux ratios of asymmetric FPs were consistent (within a factor of 2) with the predictions from asymmetric column densities. While that scenario may apply to those flares, we should note that their broad band *Yohkoh* observations set less stringent constraints than our high resolution *RHESSI* observations, which can lead to different conclusions. In particular, their analyses were limited to images in the M1 (23–33 keV) and M2 (33–55 keV) bands, where the column density effect is more pronounced and contaminated from thermal emission is possible, while our observations cover a higher and wider energy range of 50–150 keV.

5.3. *Magnetic Mirroring and Column Density Combined*

We have seen from the above discussions that each of the two transport effects *alone* can only explain to some extent the observed FP asymmetries: (1) Asymmetric magnetic mirroring is consistent with the asymmetric HXR fluxes in the average sense of the flare duration, but it has difficulties in accounting for the flux asymmetry later in the flare. (2) Asymmetric column densities in the two legs of the flare loop are qualitatively consistent with the asymmetric HXR fluxes, but their quantitative predictions of fluxes and spectral hardness contradict the observations. These two transport effects, in reality, operate at the *same time*, because electrons experience Coulomb collisions while being mirrored back and forth in the loop, and thus the collisionless (adiabatic) assumption that we adopted earlier for simplicity for magnetic mirroring needs to be dropped. In particular, since W-FP has stronger mirroring (than E-FP), the average pitch angle of electrons impinging there is larger, and thus the effective column density $N_{\text{tr, eff}} = N_{\text{tr}}/\langle\mu\rangle$ is greater than previously thought. This can enhance the column density asymmetry. In what follows, we attempt to provide an explanation for some aspects of the observations by combining the two effects.

From the above discussion and the observations presented in § 4, we should pay attention to the distinction between the two HXR peaks. As shown in Figure 9*c*, during Peak 1 ($< t_2$=20:48 UT) the FP HXR flux asymmetry seems to be mainly controlled by magnetic mirroring, while during Peak 2 ($> t_2$), especially after the HXR maximum at t_3=20:51 UT, this control seemingly fails. A viable explanation for the two-peak distinction is that (1) at early times, the densities (Fig. 6*d*) and lengths (Fig. 8*a*) of the loops are small, resulting in small coronal column densities (Fig. 9*e*) from the acceleration site to the FPs. Energy losses and pitch-angle scattering due

to Coulomb collisions are less important, and therefore the rates of electron precipitation to the FPs are mainly governed by mirroring. (2) Later in the flare, as the loop densities and lengths have increased considerably, the column densities become larger and the collisional effects become more important than before in shaping the observed FP flux asymmetry. In addition, since magnetic mirroring depends on the gradient $d \ln B/dN$ (e.g., Leach & Petrosian 1981), this effect becomes less important when the column density N increases faster than the relative change of magnetic field from the LT to the FP, which is possibly the case later in the flare. Therefore, at later times, the prediction of magnetic mirroring alone tends to deviate from the data, which might be explained by the two transport effects combined. The outcome of the combination can be modeled quantitatively as discussed later in § 6 for future work.

There are several coincidences with the two-peak division which seem to have causal connections: (1) As noted in § 4.1, the correlation between the HXR fluxes and spectral indexes (Figs. 9a and 9d) can be described as common "soft-hard-soft" during Peak 1 and as "soft-hard-hard" during Peak 2. The spectral hardening at later times may be associated with the increasing loop column densities (Fig. 9e), due to collision-caused hardening mentioned above (§5.2). (2) During Peak 1, the magnetic fields at the two FPs are weakly correlated with each other (Fig. 9b), while this correlation becomes progressively nonexistent during Peak 2, especially after its maximum t_3=20:51 UT, possibly because of longer loops. (3) The transition (t_2=20:48 UT) between the two HXR peaks coincides with the sudden jump in the positions of both FPs (Figs. 7a and 8e), the dip in the loop length (Fig. 8a), and the valley in the magnetic field strengths (Fig. 9b). This points to the start of the new episode of energy release of Peak 2, presumably associated with a new series of loops that have physical conditions different from those in Peak 1. This transition may be related to the different behaviors of magnetic mirroring during the two peaks noted above.

5.4. *Discussion on Other Asymmetry-causing Effects*

Here we briefly discuss transport effects other than magnetic mirroring and column density, and acceleration related effects that can contribute to the observed HXR flux and spectral asymmetries.

Asymmetry during the *transport process* — (1) **Non-uniform target ionization**: In the above analysis we assumed a fully ionized background in the path of high-energy electrons, but in reality the background targets vary from fully ionized in the corona to neutral in the chromosphere. The presence of neutral atoms reduces the rates of long-range collisional energy losses and pitch-angle scattering and thus increases the bremsstrahlung efficiency (Brown 1973; Leach & Petrosian 1981; Kontar et al. 2002). In this flare, at the E-FP with weaker magnetic mirroring electrons can penetrate deeper into the chromosphere and thus encounter more neutral atoms. This may result in a higher HXR flux and harder spectrum in the 50–150 keV range at E-FP than at W-FP, qualitatively consistent with the observations. (2) **Relativistic beaming and photospheric albedo**: At the E-FP with weaker mirroring, the angular distribution of electrons are more con-

centrated to the forward direction down to the photosphere. When the FPs are seen on the solar disk from above, the increasing importance with energy of the forward relativistic beaming effect (McTiernan & Petrosian 1991) results in a smaller fraction of high-energy photons emitted upward at E-FP. Meanwhile, since relatively more photons are (beamed) emitted downward at E-FP, albedo or Compton back-scattering (Langer & Petrosian 1977; Bai & Ramaty 1978) is stronger there. Both effects can cause a softer X-ray spectrum at E-FP than at W-FP, competing with other effects mentioned above, which may explain why the spectral indexes are so close ($\langle \gamma_2 \rangle - \langle \gamma_1 \rangle = 0.15 \pm 0.13$). (3) **Return currents** and the associated electric field decrease the energy of the downward-streaming electrons, with the major impact being on the lower-energy electrons (Zharkova & Gordovskyy 2006). Different precipitating electron beam fluxes in the two legs of the flare loop may induce different return current densities, and thus can result in different HXR fluxes and spectral shapes at the two FPs.

Intrinsic asymmetry arising from the particle *acceleration process* — An energy-dependent FP HXR flux asymmetry ($|A|$, eq. [1]), which has a maximum in the intermediate energy range (20–40 keV) and decreases toward both low and high energies, was found by Alexander & Metcalf (2002). This was attributed to an asymmetric, energy-dependent accelerator from which more electrons are injected preferentially into one of the two legs of the loop (McClements & Alexander 2005). Asymmetric electron beams can be produced by the electric field in a reconnection current sheet (Zharkova & Gordovskyy 2004). For the flare under study no reliable asymmetry can be obtained below 50 keV due to pulse pileup; above 50 keV asymmetry either increases with energy (see the flux ratio in Fig. 5b) or remains constant, opposite to the decreasing asymmetry reported by Alexander & Metcalf (2002) in this energy range. From *Yohkoh* HXT data Aschwanden et al. (1999) also found no general energy-dependent pattern of flux asymmetry. Furthermore, if acceleration by plasma waves is the dominant mechanism, it is difficult to realize an asymmetric particle accelerator in the turbulence region due to frequent scatterings. Whether the scenario proposed by McClements & Alexander (2005) is the rule or an exception thus remains an open question.

6. SUMMARY AND CONCLUSION

We have presented imaging and spectral analysis of the *RHESSI* observations of the 2003 October 29 X10 flare showing two conjugate HXR footpoints (FPs), which are well-defined during the bulk of the flare duration. One FP lies to the east (E-FP) and the other to the west (W-FP) of the north-south magnetic neutral line (NL). This flare provides a unique opportunity to study in great detail the spatial, temporal, and spectral properties of the FPs and their associated magnetic fields. The impulsive phase was relatively long ($\sim$20 minutes), HXR fluxes were detected by *RHESSI* at energies up to hundreds of keV, and it was located close to disk center, resulting in minimum projection effects and excellent magnetic field measurements from *SOHO* MDI. Our main findings regarding the unshearing motions, various correlations, and asymmetric characteristics of the two FPs are as follows.

1. **Two-phase FP unshearing and loop-top (LT) motions** are observed in this flare. In Phase I the two identified FPs become closer to each other as they rapidly move almost anti-parallel to the magnetic NL, while in Phase II they move away from each other slowly, mainly perpendicular to the NL (Fig. 7a). In other words, the shear angle θ between the normal to the NL and the line connecting the two FPs exhibits a fast and then slow decrease from 56° to 12° (Fig. 8d). This suggests that later reconnected magnetic field lines are less sheared (closer to a potential field), which is consistent with early observations in HXRs and other wavelengths (e.g., Zirin & Tanaka 1973). More importantly, the transition between the two phases coincides with the direction reversal of the apparent motion of the LT source along the NL (Fig. 8b), and the minima of the estimated loop length (Fig. 8a) and LT height (Fig. 8b). This suggests that the *initial decrease* of the LT altitude observed in many other *RHESSI* flares (e.g., Sui & Holman 2003) may be associated with shorter loops during the *fast unshearing* motion phase when the reconnection site propagates along the arcade. A possible explanation for this early phase is the implosion conjecture (Hudson 2000) that predicts contraction of field lines during a solar explosion including flares and CMEs.

2. There are **correlations** among the temporal evolutions of various quantities (Table 2), some of which exhibit distinctions between the two HXR peaks (division at 20:48 UT): (a) The HXR fluxes (Figs. 9a and 10a) and spectral indexes (Figs. 9c and 10b) of the two FPs are strongly correlated. This is evidence that the two HXR sources are from conjugate FPs at the two ends of the same magnetic loop. (b) The HXR flux and spectral index of each FP show a commonly observed "soft-hard-soft" evolution (Figs. 9a, 9d, and 10c) during HXR Peak 1, while during Peak 2 the evolution becomes "soft-hard-hard". (c) The magnetic field strengths at the two FPs also exhibit some temporal correlation (Figs. 9b and 10d) particularly during Peak 1, consistent with the conjugate FPs identification. (d) The FP HXR fluxes exponentially correlates with the magnetic field strengths (Figs. 10e and 10f), which also anti-correlates with the spectral indexes during Peak 1. These correlations suggest that stronger magnetic fields, and/or larger reconnection rates or larger electric fields in the reconnection region are responsible for producing larger fluxes and harder spectra for the accelerated electrons and thus the resulting HXRs. This is in qualitative agreement with the predictions of the stochastic acceleration model (Petrosian & Liu 2004) and the electric field acceleration model (Holman 1985).

3. Various **asymmetries** are observed between the conjugate FPs (Table 3): (a) On average, the eastern footpoint (E-FP) HXR flux is 2.2 times higher than that of the western footpoint (W-FP; Fig. 9a), while its magnetic field strength is 1.8 times weaker (520 G vs. 960 G; Fig. 9b). This is consistent with asymmetric magnetic mirroring (§5.1). (b) The average estimated coronal column density from the edge of the LT source (assumed to be the acceleration region) to the transition region at E-FP is 1.7 times smaller than that of W-FP (1.2×10^{20} vs. 2.1×10^{20} cm^{-2}; Fig. 9e). This qualitatively agrees with the HXR flux asymmetry, because a larger coronal column density results in more

HXRs produced in the loop legs and thus less HXRs emitted from the FP below the transition region, especially at low energies (Fig. 11; §5.2). (c) The photon spectra above 50 keV of the two FPs are almost parallel to each other (Fig. 5a), with the brighter E-FP being consistently slightly harder than the dimmer W-FP (Fig. 9d). Their mean index values $\langle\gamma_1\rangle = 3.63 \pm 0.06$ and $\langle\gamma_2\rangle = 3.79 \pm 0.11$ have a marginally significant difference of $\langle\gamma_2\rangle - \langle\gamma_1\rangle = 0.15 \pm 0.13$. In other words, the W-to-E ratio of the photon fluxes is a constant or a slightly decreasing function of energy. This contradicts the column density effect which would produce a harder spectrum at the dimmer W-FP (Fig. 11). (d) As expected from asymmetric magnetic mirroring, there is a temporal correlation between the W-to-E HXR flux ratio and the E-to-W magnetic field ratio. However, this correlation only holds during HXR Peak 1 but gradually breaks down during Peak 2 (Figs. 9c). We suggest that a combination of the asymmetric magnetic mirroring and column density effects could explain this variation (§5.3). Specifically, since the column densities in later formed loops are larger (Fig. 9e), collisions are more important at later times, making the HXR flux ratio deviate from the prediction of mirroring alone.

In our analysis we have treated the magnetic mirroring and column density effects separately in order to make the problem analytically tractable, yet without loss of the essential physics. However, in reality, the two effects are coupled and they should be studied together self-consistently to obtain a quantitative model prediction. This is done with the Fokker-Planck particle transport model of Leach & Petrosian (1981) in a converging magnetic field geometry. Results from such an analysis will be presented in a future publication. In addition to numerical modeling, we have started a statistical study of *RHESSI* flares showing double FP sources that are close to disk center and thus have less projection effects. We hope to conduct future joint observations with *RHESSI*, *Hinode*, and the *Solar Dynamic Observatory* to obtain more advanced measurements of the magnetic fields at FPs. These future investigations will help improve our understanding of the underlying physics of asymmetric HXR FPs.

APPENDIX

A. EFFECTS OF PULSE PILEUP ON IMAGING SPECTROSCOPY

Pulse pileup refers to the phenomenon that two or more photons close in time are detected as one photon with their energies summed (Smith et al. 2002). When count rates are high, as happens in large flares, an artifact appears in the measured spectrum at twice or a higher multiple of the energy of the peak of the count rate spectrum that is at ∼6 keV in the *RHESSI* attenuator A0 state, ∼10 keV in the A1 state, and ∼18 keV in the A3 state. Due to nonlinear complexity, there is currently no 100% reliable pileup correction algorithm available in the *RHESSI* software, especially for imaging spectroscopy. Here we have adopted and improved upon the methods used by Liu et al. (2006b, their §2.1) to estimate the pileup importance and minimize its effects on our analysis.

A general indicator of pileup severity is the livetime, the complement of the deadtime during which the detector is not able to distinguish among different incident photons. We find that the fractional livetime averaged over detectors 3–9 and over 4 s intervals has a V-shaped time profile (not shown) with values ≥90% at the beginning (<20:40 UT) and end (>21:00 UT) of the flare, and a minimum of 24% at 20:46:10 UT during the impulsive peak. This value is very small compared with the livetime minima of 55% during the 2002 July 23 X4.8 flare and 94% during the 2002 February 20 C7.5 flare, and indicates severe pileup effects. On much shorter time scales, the livetime fluctuates in anti-correlation with the count rate due to the modulation of the *RHESSI* grids during the spacecraft rotation, and a variation between 5% and 70% is found for detector 9 at 20:46:10 UT. Such fine temporal variations make pileup correction for imaging spectroscopy even more difficult than for spatially integrated spectroscopy.

Schwartz (2008) has recently developed a forward-modeling tool to simulate pileup effects for imaging spectroscopy, based on input model images consisting of sources of user-specified spectra and spatial distributions. This tool has been applied here to generate simulated images at 20:46:00–20:46:04 UT (near the livetime minimum) using the real flight instrument response. The model image consists of a thermal elliptic-gaussian LT source and two nonthermal (power-law) circular-gaussian FP sources, whose geometric and spectral parameters were selected to match the observation at 20:46:00–20:46:20 UT. We have run simulations for four cases as listed in Table 4 with different count rates corresponding to different levels of pileup. Case A returns the nominal result assuming no pileup at all; Case C represents this flare with the count rate of CR$= 1.1 \times 10^5$ (counts s^{-1} detector^{-1}) identical to the maximum of the measured value at 20:46:10 UT. In each case images in 16 energy bins (used in §2.2) from 6 to 150 keV were reconstructed and then *normalized* as if their corresponding count rates were identical to the measured value. The final normalization makes different cases directly comparable and emphasizes the effects of pileup.

TABLE 4

SIMULATED EFFECTS OF PULSE PILEUP AT DIFFERENT LEVELS (INDICATED BY THE COUNT RATES) ON IMAGING SPECTROSCOPY. THE HIGHEST COUNT RATE DURING THIS FLARE IS CR$_{\rm obs}$ = 1.1×10^5 COUNTS S^{-1} DETECTOR^{-1}. THE FLUXES AND EMS ARE *normalized* BY A FACTOR OF CR$_{\rm obs}$/CR, WHERE CR IS THE COUNT RATE ASSIGNED TO EACH CASE.

Case	Count Rate (CR) (cts s^{-1} det^{-1})	FP spectral index in 50–150 keV			FP flux at 50 keV (ph s^{-1} cm^{-2} keV^{-1})			LT spectral parameters in 6–20 keV	
(Subscript 1: E-FP, 2: W-FP)		γ_1	γ_2	$\gamma_2 - \gamma_1$	I_1	I_2	I_2/I_1	EM (10^{49} cm^{-3})	T (MK)
A	7.7×10^4 (but no pileup)	3.71	3.82	0.11	25.5	12.0	0.47	15.4	30.8
B	1.6×10^4	3.74	3.85	0.11	29.2	13.7	0.47	15.0	30.9
C	1.1×10^5 (measured)	3.85	3.93	0.08	52.8	24.0	0.46	12.1	31.0
D	3.9×10^5	3.66	3.71	0.05	134	58.9	0.44	6.64	31.1

Let us first examine the effects of pileup on source *morphology*. From Figure 12 we find the following features in agreement with the speculation of Liu et al. (2006b, their §2.1): (1) The source positions, shapes, and sizes are generally well preserved, especially at low and high energies. This is because photons from the same region within the FWHM resolution of a grid have higher probability to pileup as one count in the underlying detector than photons from different regions. Therefore during image reconstruction piled-up photons are likely to be registered back to their original source. (2) The main visible artifact is the "ghost" LT source at intermediate energies (e.g., 34–41 keV). This is because the count-rate spectrum of this flare (in attenuator state A3) is ∼18 keV at which the LT source dominates over the FP sources, and twice this energy is 36 keV where the first-order pileup is most pronounce.

Next we check the effects of pileup on source *spectra*. In general, pileup shifts photons from low energies to high energies, as can be seen from Figures 13a and 13b. For the LT source, the spectrum is only slightly reduced at low energies (≲20 keV), with negligible changes in shape, while it is substantially altered in both normalization and shape at high energies. The opposite is true for the E-FP source whose spectrum ≳50 keV is only elevated by a roughly constant factor independent of energy (with minimal changes in slope). For comparison, we also performed pileup correction to the spatially integrated spectrum at 20:46:00–20:46:20 UT using the preliminary algorithm of Smith et al. (2002) with a tweak factor of 0.6. The result shown in Figures 13c and 13d. Because the LT source dominates at low energies, while the FPs dominate at high energies, the above mentioned features at these extreme energies are evident. The most obvious alteration of the spectrum shape occurs in the 30–40 keV range that covers twice the peak energy (18 keV) of the count-rate spectrum.
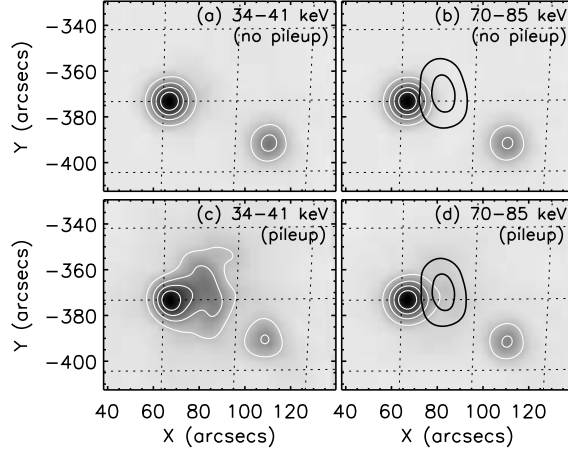
FIG. 12.— Simulated images for 20:46:00–20:46:04 UT at different energies. (*a*) and (*b*) Case A without pileup. (*c*) and (*d*) Case C with pileup representing this flare. The dark contours at 40% and 80% of the maximum in (*b*) and (*d*) represent the 6–8 keV image where the LT source dominates.
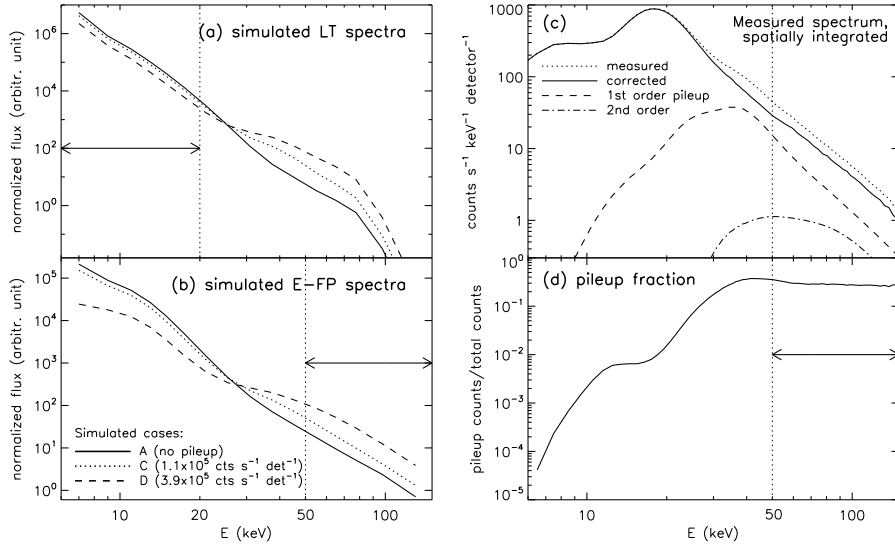

FIG. 13.— *Left:* Simulated photon spectra for the LT (*a*) and E-FP sources (*b*) for Cases A, C, and D at 20:46:00–20:46:04 UT. The excessive LT flux $\gtrsim$30 keV and E-FP flux $\lesssim$30 keV are due to the spatial overlap of the two sources. *Right:* Measured, spatially integrated, count rate spectrum (*c*) averaged over detectors 3–9 for interval 20:46:00–20:46:20 UT before and after pileup correction (Smith et al. 2002). The broken lines are the estimated first- (two photons) and second-order (three photons) piled-up spectra, with their peaks marked by the vertical dotted lines. (*d*) The fraction of the total recorded counts that are piled up (including first- and second-order). The double arrows indicate the energy ranges used in the analysis.

We repeated our imaging spectroscopy analysis here on the simulated data and the results are summarized in Table 4. The striking feature is that the *spectral shapes* are well preserved across a wide range of pileup severity, as indicated by (1) the temperature T inferred from the LT spectra <20 keV and (2) the spectral indexes γ_1 and γ_2 and their difference, and the flux ratio I_2/I_1 inferred from the FP spectra >50 keV. The FP portion of these spectral parameters are of our main interest in this paper. As to the *absolute normalizations*, according to Case C, the estimated FP fluxes can be elevated by a factor of 2 and the EM can be reduced by 20% for this flare. These are the upper limits of changes as we used here the maximum observed count rate at 20:46:10 UT, and the changes are reduced considerably away from this time. The effects on the FP spectra are further reduced later in the flare as the spatial contamination from the LT is alleviated when the FP sources move away. We conclude that our choice of fitting the LT spectra only below 20 keV and the FP spectra only above 50 keV is justified and has effectively minimized pileup effects on our analysis. We note in passing that the count spectrum of radiation belt particles estimated in § 2.1 appears as a hump peaking at ∼50 keV and the counts integrated in the 3–600 keV band amount to only <8% of the total counts during 20:40–21:05 UT. Therefore these particles have a negligible contribution to pileup.

B. COALIGNMENT OF IMAGES OBTAINED BY DIFFERENT INSTRUMENTS

We describe here how we coaligned the *RHESSI* images and *SOHO* MDI magnetograms presented in this paper. (See a general tutorial: http://hesperia.gsfc.nasa.gov/~ptg/trace-align.) *RHESSI*'s images are located on the Sun to sub-arcsecond accuracy thanks to its solar limb sensing aspect system and star based roll angle measurements (Fivian et al. 2002). MDI images had accurate plate scales and their roll angles were corrected for the solar P-angle,

but had different absolute origins for the solar x and y coordinates. MDI images were corrected to match the *RHESSI* features using the following procedures.

(1) The first step is to identify specific features on the MDI map that have *RHESSI* counterparts. Qiu & Gary (2003) found good spatial agreement between HXR FPs and MDI magnetic anomaly features with an apparent sign reversal in a white-light flare. This was interpreted as HXR-producing nonthermal electrons being responsible for heating the lower atmosphere, which consequently altered the Ni I 6768 Å line profile that is used by MDI to measure the magnetic field.

We selected two neighboring magnetograms at 20:41:35 and 20:42:35 UT when the magnetic anomaly features were most pronounced, and subtracted the former from the latter. This running-differenced map (which we call map_0, Fig. 14) highlights regions of the newest changes, which are presumably caused by precipitation of nonthermal electrons and are expected to appear cospatial with HXR sources. As evident, there is one (three) apparent increase (decrease) feature(s) mainly in the negative (positive) polarity (cf., Fig. 7), which appear as *white (dark)* patches in Figure 14. Meanwhile, we reconstructed a *RHESSI* image (called map_1) at 60–120 keV integrated in the interval of 20:42:19–20:42:51 UT (a multiple of the *RHESSI* spin period, ~ 4 s, and closest to the corresponding integration time of the second MDI magnetogram, 20:42:20–20:42:50 UT). We found an one-to-one correspondence between the four major HXR FP sources (Fig. 14, *contours*) and the magnetic anomalies.

(2) We then converted *SOHO*'s L1 view to the appearance as viewed from an Earth orbit, and we call the resulting differenced MDI magnetogram $map_{0,\,\mathrm{Earth}}$.

(3) Finally, we took the absolute value of MDI $map_{0,\,\mathrm{Earth}}$ to make a new map called $map'_{0,\,\mathrm{Earth}}$ and coregister it with *RHESSI* map_1 by cross-correlation. The required shifts for $map'_{0,\,\mathrm{Earth}}$ are $\Delta x = 4.5'' \pm 2.0''$ and $\Delta y = -2.8'' \pm 2.0''$, where the $2.0''$ uncertainty was estimated with the MDI pixel size.
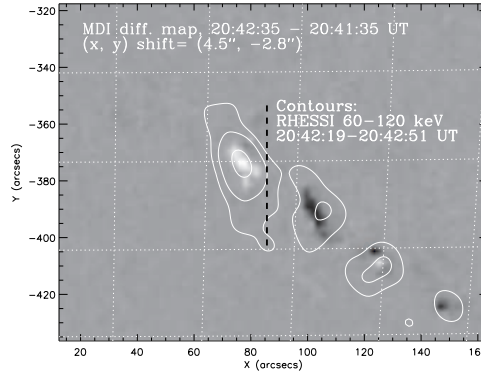

FIG. 14.— Difference (*gray background*) between two MDI magnetograms at 20:42:35 and 20:41:35 UT, overlaid with a *RHESSI* 60–120 keV image at 20:42:19–20:42:51 UT (white contours at 15%, 30%, & 80% of the maximum brightness). The MDI map has been corrected to an Earth-centered view and shifted in x and y to best match the four *RHESSI* HXR sources (see text). The dark dashed line is the same simplified magnetic NL shown in Fig. 7*a*.

C. DERIVATION OF FOOTPOINT HXR FLUXES RESULTING FROM ASYMMETRIC CORONAL COLUMN DENSITIES

Here we derive the numerical expressions for the HXR fluxes of the two FPs and their ratio as a function of energy resulting from column density asymmetry addressed in § 5.2. We adopted the empirical expression of Leach & Petrosian (1983, their eq. 11) for nonthermal bremsstrahlung X-ray emission as a function of column density. This expression well approximates the Fokker-Planck calculation of particle transport under the influence of Coulomb collisions that includes energy losses and pitch-angle scattering, the latter of which was neglected in other forms of X-ray profiles based on approximate analytical solutions (e.g., Emslie & Machado 1987). For an injected power-law (index δ) electron flux, the resulting fractional bremsstrahlung emission intensity per unit dimensionless column density τ at photon energy k (in units of rest electron energy $m_e c^2 = 511$ keV, m_e being the electron mass) can be written as

$$I_0(\tau, k) = \left(\frac{\delta}{2} - 1\right)\left(\frac{k+1}{gk^2}\right)\left(1 + \tau \frac{k+1}{gk^2}\right)^{-\delta/2}, \tag{C1}$$

where $\tau = N/[4\pi r_0^2 \ln \Lambda] = N/[5 \times 10^{22}\,\mathrm{cm}^{-2}]$ is the dimensionless column density, for the classical electron radius $r_0 = e^2/m_e c^2 = 2.8 \times 10^{-13}$ cm and the Coulomb logarithm $\ln \Lambda = 20$; g is a factor determined by the pitch-angle distribution of the injected electron spectrum, which we assumed to be isotropic and thus $g = 0.37$ (Leach 1984). This emission profile is normalized to unity, $\int_0^\infty I_0(\tau, k)d\tau = 1$. Integrating equation (C1) yields the cumulative photon emission from the injection site ($\tau = 0$) to the transition region ($\tau = \tau_{\mathrm{tr}} \equiv N_{\mathrm{tr}}/[5 \times 10^{22}\,\mathrm{cm}^{-2}]$, where $N_{\mathrm{tr}} = \int_0^{s_{\mathrm{tr}}} n[s]ds$ and s_{tr} are the coronal column density and distance to the transition region),

$$F_{\mathrm{Corona}}(\tau_{\mathrm{tr}}) = \int_0^{\tau_{\mathrm{tr}}} I_0(\tau, k)d\tau = 1 - \left(1 + \tau_{\mathrm{tr}}\frac{k+1}{gk^2}\right)^{1-\delta/2}, \tag{C2}$$

whose complement gives the emission accumulated below the transition region, i.e., the HXR flux of the FP,

$$F_{\rm FP}(\tau_{\rm tr}) = \int_{\tau_{\rm tr}}^{\infty} I_0(\tau,k)d\tau = 1 - F_{\rm Corona}(\tau_{\rm tr}) = \left(1 + \tau_{\rm tr}\frac{k+1}{gk^2}\right)^{1-\delta/2}. \quad (C3)$$

Note that at large photon energies (tens to hundreds of keV), $F_{\rm Corona}(\tau_{\rm tr})$ is usually much smaller than $F_{\rm FP}(\tau_{\rm tr})$. In addition, $F_{\rm Corona}(\tau_{\rm tr})$ is distributed in a large volume in the leg of the loop in the relatively *tenuous* plasma, while $F_{\rm FP}(\tau_{\rm tr})$ is concentrated at the FP in the *dense* transition region and chromosphere. This results in an even smaller surface brightness in the leg than at the FP, which may well exceed the dynamic range of HXR telescopes (e.g., $\gtrsim$10:1 for *RHESSI*). This is why leg emission is so rarely observed (Liu et al. 2006b; Sui et al. 2006).

As we know, a power-law electron flux (index=δ) produces a thick-target (integrated from $\tau = 0$ to $\tau = \infty$) photon spectrum of approximately a power-law, $I_{\rm thick} = A_0 k^{-\gamma}$, where $\gamma = \delta - 1$ (Brown 1971; Petrosian 1973) for an isotropically injected electron spectrum, and A_0 is the normalization factor [in units of photons s^{-1} cm^{-2} (511 keV)$^{-1}$]. Since I_0 gives the fractional spatial photon distribution at a given energy, the physical photon spectrum at energy k and at a depth where the overlying column density is τ can be written as $I(\tau,k) = I_{\rm thick}I_0(\tau,k) = A_0 k^{-\gamma}I_0(\tau,k)$. It follows that the X-ray flux of the FP is

$$I_{\rm FP}(\tau_{\rm tr},k) = \int_{\tau_{\rm tr}}^{\infty} I(\tau,k)d\tau = I_{\rm thick}F_{\rm FP}(\tau_{\rm tr}) = A_0 k^{-\gamma}\left(1 + \tau_{\rm tr}\frac{k+1}{gk^2}\right)^{1-\delta/2}, \quad (C4)$$

and the photon flux ratio of the two FPs (1 and 2),

$$R_I = \frac{I_{\rm FP}(\tau_{\rm tr,2},k)}{I_{\rm FP}(\tau_{\rm tr,1},k)} = \left(1 + \tau_{\rm tr,2}\frac{k+1}{gk^2}\right)^{1-\delta/2}\left(1 + \tau_{\rm tr,1}\frac{k+1}{gk^2}\right)^{-(1-\delta/2)}. \quad (C5)$$

The above two equations were used in § 5.2 to calculate the FP fluxes and their ratio resulting from different coronal column densities.

D. ESTIMATION OF COLUMN DENSITIES IN LOOP LEGS

We describe below the approach to estimate the coronal column densities $N_{\rm tr}$ in the legs of the loop, which is defined and used in § 5.2 as the density integrated along the loop from the acceleration region to the transition region at the FPs. In the stochastic acceleration model of Petrosian & Liu (2004), the LT source is the region where particle acceleration takes place (Liu et al. 2008; Xu et al. 2008). Assuming that this picture is true,[8] we thus subtracted[9] the estimated LT size (i.e., the radius r of the *equivalent sphere*; see Fig. 6c) from the distances along the loop from the LT centroid to the FP centroids obtained in § 4.2 (i.e., l_i, where i=1 for E-FP and 2 for W-FP; see Fig. 8a), to obtain the path lengths in the legs $s_{\rm tr,i} = l_i - r$. Here the FP centroids are assumed to be situated at negligibly small distances below the transition region. To give the desired column densities $N_{\rm tr,i}$, the path lengths $s_{\rm tr,i}$ (i=1, 2) were then multiplied by the density $n_{\rm leg}$ (assumed to be uniform) in the legs of the loop, which was estimated as follows.

The density of the LT source $n_{\rm LT}$ inferred in § 2.2 (see Fig. 6d) provides our first guess for the leg density $n_{\rm leg}$ as assumed by Falewicz & Siarkowski (2007). The relative brightness of *nonthermal* bremsstrahlung emission the leg and FP provides another important clue. This is because, for the same reason of collisional losses mentioned in § 5.2, the ratio of the leg to FP brightness, particularly at low energies, is an increasing function of the leg density. This predicted ratio cannot exceed the observed LT-to-FP brightness ratio, because the LT source is where the maximum loop brightness is located, and it includes additional contributions from *thermal* emission, piled-up photons, and/or electrons trapped in the acceleration region (Petrosian & Liu 2004). This imposes an upper limit for the leg density $n_{\rm leg}$, which we found to be $n_{\rm leg,max} = 0.5n_{\rm LT}$ based on an error and trial method. This result indicates that the average density in the legs is smaller than the estimated LT density, or that the LT density is an overestimate due to an underestimate of the volume which could result from the lack of knowledge of the source size in the third dimension along the line of sight. This leg density was then used for column densities $N_{\rm tr,i} = n_{\rm leg,max}(l_i - r)$ shown in Figure 9e.

REFERENCES

Alexander, D. & Metcalf, T. R. 2002, Sol. Phys., 210, 323
Asai, A., Ishii, T. T., Kurokawa, H., Yokoyama, T., & Shimojo, M. 2003, ApJ, 586, 624
Aschwanden, M. J. 2002, Space Science Reviews, 101, 1
Aschwanden, M. J., Fletcher, L., Sakao, T., Kosugi, T., & Hudson, H. 1999, ApJ, 517, 977
Aschwanden, M. J., Schwartz, R. A., & Alt, D. M. 1995, ApJ, 447, 923
Bai, T. & Ramaty, R. 1978, ApJ, 219, 705
Battaglia, M. & Benz, A. O. 2006, A&A, 456, 751
Benka, S. G. & Holman, G. D. 1994, ApJ, 435, 469

Bogachev, S. A., Somov, B. V., Kosugi, T., & Sakao, T. 2005, ApJ, 630, 561
Brown, J. C. 1971, Sol. Phys., 18, 489
—. 1973, Sol. Phys., 28, 151
Carmichael, H. 1964, in The Physics of Solar Flares, ed. W. N. Hess, 451
Donea, A.-C. & Lindsey, C. 2005, ApJ, 630, 1168
Emslie, A. G., Kontar, E. P., Krucker, S., & Lin, R. P. 2003, ApJ, 595, L107
Emslie, A. G. & Machado, M. E. 1987, Sol. Phys., 107, 263
Falewicz, R. & Siarkowski, M. 2007, A&A, 461, 285

[8] In the competing model of Fletcher & Hudson (2008), acceleration by plasma waves takes place near/at the chromosphere. In such a case, our density estimation here must be modified.

[9] There are observations (e.g., Masuda et al. 1994; Aschwanden et al. 1995) suggestive that the acceleration region is located above the SXR loop, and in that case a distance needs to be added to l_i. Such a practice was not attempted here, and as we can see from § 5.2, will not change our conclusions.

Fivian, M., Hemmeck, R., McHedlishvili, A., & Zehnder, A. 2002, Sol. Phys., 210, 87

Fletcher, L. & Hudson, H. S. 2001, Sol. Phys., 204, 69

—. 2002, Sol. Phys., 210, 307

—. 2008, ApJ, 675, 1645

Forbes, T. G. & Acton, L. W. 1996, ApJ, 459, 330

Forbes, T. G. & Lin, J. 2000, Journal of Atmospheric and Terrestrial Physics, 62, 1499

Gallagher, P. T., Dennis, B. R., Krucker, S., Schwartz, R. A., & Tolbert, A. K. 2002, Sol. Phys., 210, 341

Gary, D. E. & Hurford, G. J. 1990, ApJ, 361, 290

Goff, C. P., Matthews, S. A., van Driel-Gesztelyi, L., & Harra, L. K. 2004, A&A, 423, 363

Gopalswamy, N., Barbieri, L., Cliver, E. W., Lu, G., Plunkett, S. P., & Skoug, R. M. 2005, J. Geophys. Res., 110, 9

Grigis, P. C. & Benz, A. O. 2005, ApJ, 625, L143

Hagyard, M. J., Teuber, D., West, E. A., & Smith, J. B. 1984, Sol. Phys., 91, 115

Hannah, I. G. & Fletcher, L. 2006, Sol. Phys., 236, 59

Hirayama, T. 1974, Sol. Phys., 34, 323

Holman, G. D. 1985, ApJ, 293, 584

—. 2003, ApJ, 586, 606

Holman, G. D., Sui, L., Brosius, D. G., & Dennis, B. R. 2005, AGU Fall Meeting Abstracts, A288

Hoyng, P., Duijveman, A., Machado, M. E., Rust, D. M., Svestka, Z., Boelee, A., de Jager, C., Frost, K. T., Lafleur, H., Simnett, G. M., van Beek, H. F., & Woodgate, B. E. 1981, ApJ, 246, L155

Hudson, H. S. 2000, ApJ, 531, L75

Hurford, G. J., Krucker, S., Lin, R. P., Schwartz, R. A., Share, G. H., & Smith, D. M. 2006, ApJ, 644, L93

Hurford, G. J., Schmahl, E. J., Schwartz, R. A., Conway, A. J., Aschwanden, M. J., Csillaghy, A., Dennis, B. R., Johns-Krull, C., et al. 2002, Sol. Phys., 210, 61

Ji, H., Huang, G., & Wang, H. 2007, ApJ, 660, 893

Ji, H., Huang, G., Wang, H., Zhou, T., Li, Y., Zhang, Y., & Song, M. 2006, ApJ, 636, L173

Ji, H., Wang, H., Liu, C., & Dennis, B. R. 2008, ApJ, 680, 734

Jiang, Y. W., Liu, S., Liu, W., & Petrosian, V. 2006, ApJ, 638, 1140

Jin, M. & Ding, M. D. 2007, A&A, 471, 705

Kane, S. R. & Anderson, K. A. 1970, ApJ, 162, 1003

Kiplinger, A. L. 1995, ApJ, 453, 973

Kliem, B., Karlický, M., & Benz, A. O. 2000, A&A, 360, 715

Kontar, E. P., Brown, J. C., & McArthur, G. K. 2002, Sol. Phys., 210, 419

Kopp, R. A. & Pneuman, G. W. 1976, Sol. Phys., 50, 85

Krucker, S., Fivian, M. D., & Lin, R. P. 2005, Advances in Space Research, 35, 1707

Krucker, S., Hurford, G. J., & Lin, R. P. 2003, ApJ, 595, L103

Krucker, S., Kontar, E. P., Christe, S., & Lin, R. P. 2007, ApJ, 663, L109

Kundu, M. R., Nitta, N., White, S. M., Shibasaki, K., Enome, S., Sakao, T., Kosugi, T., & Sakurai, T. 1995, ApJ, 454, 522

Langer, S. H. & Petrosian, V. 1977, ApJ, 215, 666

Leach, J. 1984, Ph.D. Thesis, Stanford University

Leach, J. & Petrosian, V. 1981, ApJ, 251, 781

—. 1983, ApJ, 269, 715

Li, J., Metcalf, T. R., Canfield, R. C., Wuelser, J.-P., & Kosugi, T. 1997, ApJ, 482, 490

Li, J. P. & Ding, M. D. 2004, ApJ, 606, 583

Li, Y. P. & Gan, W. Q. 2005, ApJ, 629, L137

—. 2006, ApJ, 644, L97

Liu, C., Lee, J., Deng, N., Gary, D. E., & Wang, H. 2006a, ApJ, 642, 1205

Liu, S., Petrosian, V., & Mason, G. M. 2004a, ApJ, 613, L81

Liu, W. 2006, PhD thesis, Stanford University

Liu, W., Jiang, Y. W., Liu, S., & Petrosian, V. 2004b, ApJ, 611, L53

Liu, W., Jiang, Y. W., Liu, S., & Petrosian, V. 2004c, in Bulletin of the American Astronomical Society, Vol. 36, 739

Liu, W., Liu, S., Jiang, Y. W., & Petrosian, V. 2006b, ApJ, 649, 1124

Liu, W., Petrosian, V., Dennis, B. R., & Jiang, Y. W. 2008, ApJ, 676, 704

Liu, Y. & Hayashi, K. 2006, ApJ, 640, 1135

Liu, Y., Kurokawa, H., Liu, C., Brooks, D. H., Dun, J., Ishii, T. T., & Zhang, H. 2007, Sol. Phys., 240, 253

Masuda, S., Kosugi, T., Hara, H., Tsuneta, S., & Ogawara, Y. 1994, Nature, 371, 495

Masuda, S., Kosugi, T., & Hudson, H. S. 2001, Sol. Phys., 204, 55

McClements, K. G. & Alexander, D. 2005, ApJ, 619, 1153

McTiernan, J. M. & Petrosian, V. 1991, ApJ, 379, 381

Melrose, D. B. & White, S. M. 1979, Proceedings of the Astronomical Society of Australia, 3, 369

—. 1981, J. Geophys. Res., 86, 2183

Metcalf, T. R., Leka, K. D., & Mickey, D. L. 2005, ApJ, 623, L53

Miller, J. A., Cargill, P. J., Emslie, A. G., et al. 1997, J. Geophys. Res., 102, 14631

Moore, R. L., Sterling, A. C., Hudson, H. S., & Lemen, J. R. 2001, ApJ, 552, 833

Pallavicini, R., Vaiana, G. S., Kahler, S. W., & Krieger, A. S. 1975, Sol. Phys., 45, 411

Parks, G. K. & Winckler, J. R. 1969, ApJ, 155, L117

Petrosian, V. 1973, ApJ, 186, 291

Petrosian, V., Donaghy, T. Q., & McTiernan, J. M. 2002, ApJ, 569, 459

Petrosian, V. & Liu, S. 2004, ApJ, 610, 550

Petschek, H. E. 1964, in The Physics of Solar Flares, ed. W. N. Hess, 425

Qiu, J., Ding, M. D., Wang, H., Gallagher, P. T., Sato, J., Denker, C., & Goode, P. R. 2001, ApJ, 554, 445

Qiu, J. & Gary, D. E. 2003, ApJ, 599, 615

Qiu, J., Lee, J., Gary, D. E., & Wang, H. 2002, ApJ, 565, 1335

Reeves, K. K., Seaton, D. B., & Forbes, T. G. 2008, ApJ, 675, 868

Rust, D. M. & Bar, V. 1973, Sol. Phys., 33, 445

Saint-Hilaire, P., Krucker, S., & Lin, R. P. 2008, Sol. Phys., 250, 53

Sakao, T. 1994, PhD thesis, University of Tokyo

Sakao, T., Kosugi, T., & Masuda, S. 1998, in ASSL Vol. 229: Observational Plasma Astrophysics: Five Years of Yohkoh and Beyond, ed. T. Watanabe & T. Kosugi (Boston: Kluwer), 273

Saldanha, R., Krucker, S., & Lin, R. P. 2008, ApJ, 673, 1169

Schmahl, E. J., Kundu, M. R., & Garaimov, V. I. 2006, ApJ, 643, 1271

Schrijver, C. J., Hudson, H. S., Murphy, R. J., Share, G. H., & Tarbell, T. D. 2006, ApJ, 650, 1184

Schwartz, R. A. 2008, AGU Spring Meeting Abstracts, B3+

Siarkowski, M. & Falewicz, R. 2004, A&A, 428, 219

Smith, D. M., Lin, R. P., Turin, P., Curtis, D. W., Primbsch, J. H., Campbell, R. D., Abiad, R., Schroeder, P., et al. 2002, Sol. Phys., 210, 33

Somov, B. V., Kosugi, T., Hudson, H. S., Sakao, T., & Masuda, S. 2002, ApJ, 579, 863

Sturrock, P. A. 1966, Nature, 211, 695

Su, Y., Golub, L., & Van Ballegooijen, A. A. 2007, ApJ, 655, 606

Sudol, J. J. & Harvey, J. W. 2005, ApJ, 635, 647

Sui, L. & Holman, G. D. 2003, ApJ, 596, L251

Sui, L., Holman, G. D., & Dennis, B. R. 2004, ApJ, 612, 546

—. 2006, ApJ, 645, L157

Švestka, Z. 1976, Solar Flares (Berlin, Heidelberg: Springer-Verlag, ISBN 90-277-0662-X, 415 p.)

Švestka, Z. F., Fontenla, J. M., Machado, M. E., Martin, S. F., & Neidig, D. F. 1987, Sol. Phys., 108, 237

Tanaka, K. 1987, PASJ, 39, 1

Tsuneta, S., Hara, H., Shimizu, T., Acton, L. W., Strong, K. T., Hudson, H. S., & Ogawara, Y. 1992, PASJ, 44, L63

Veronig, A. M., Karlický, M., Vršnak, B., Temmer, M., Magdalenić, J., Dennis, B. R., Otruba, W., & Pötzi, W. 2006, A&A, 446, 675

Vršnak, B., Temmer, M., Veronig, A., Karlický, M., & Lin, J. 2006, Sol. Phys., 234, 273

Wang, H., Gary, D. E., Zirin, H., Schwartz, R. A., Sakao, T., Kosugi, T., & Shibata, K. 1995, ApJ, 453, 505

Wang, H., Spirock, T. J., Qiu, J., Ji, H., Yurchyshyn, V., Moon, Y.-J., Denker, C., & Goode, P. R. 2002, ApJ, 576, 497

Wang, J., Shibata, K., Nitta, N., Slater, G. L., Savy, S. K., & Ogawara, Y. 1997, ApJ, 478, L41+

Xu, Y., Cao, W., Liu, C., Yang, G., Jing, J., Denker, C., Emslie, A. G., & Wang, H. 2006, ApJ, 641, 1210

Xu, Y., Cao, W., Liu, C., Yang, G., Qiu, J., Jing, J., Denker, C., & Wang, H. 2004, ApJ, 607, L131

Xu, Y., Emslie, A. G., & Hurford, G. J. 2008, ApJ, 673, 576

Yang, G., Xu, Y., Cao, W., Wang, H., Denker, C., & Rimmele, T. R. 2004, ApJ, 617, L151

Young, P. R., Del Zanna, G., Landi, E., Dere, K. P., Mason, H. E., & Landini, M. 2003, ApJS, 144, 135

Zharkova, V. V. & Gordovskyy, M. 2004, ApJ, 604, 884
—. 2006, ApJ, 651, 553

Zirin, H. & Tanaka, K. 1973, Sol. Phys., 32, 173